ASSESSMENT OF FUTURE RAINFALL PATTERNS IN CAMERON HIGHLANDS USING THE STATISTICALLY DOWNSCALED LOCAL CLIMATE MODEL

LIU NI QIAO

MASTER OF ENVIRONMENTAL TECHNOLOGY

FACULTY OF ENGINEERING AND GREEN TECHNOLOGY
UNIVERSITI TUNKU ABDUL RAHMAN

DECEMBER 2023

ASSESSMENT OF FUTURE RAINFALL PATTERNS IN CAMERON HIGHLANDS USING THE STATISTICALLY DOWNSCALED LOCAL CLIMATE MODEL

LIU NI QIAO

A thesis submitted to

Faculty of Engineering and Green Technology,

Universiti Tunku Abdul Rahman,

in partial fulfillment of the requirements for the degree of

Master of Environmental Technology

December 2023

ASSESSMENT OF FUTURE RAINFALL PATTERNS IN CAMERON HIGHLANDS USING THE STATISTICALLY DOWNSCALED LOCAL CLIMATE MODEL

ABSTRACT

Due to the disasters, such as heavy rainfall and landslides, that have occurred in Cameron Highlands in recent years, significant damage has been inflicted on public property safety and the health of the people. This study seeks to explore future precipitation changes in different scenarios and spatiotemporal contexts. The aim is to provide insights that government agencies can consider when formulating guiding principles or land-use plans. It is important to note that the scenarios presented by the local precipitation model generated in this study are merely possibilities and not definite outcomes. Research aims: 1) To develop the local climate model using the statistical downscaling approach. 2)To assess the performance of the statistically downscaled local climate model based on SSP2-4.5 and SSP5-8.5. 3). To analyse the changes in rainfall patterns (2015–2100) using spatial analysis. The study compared historical observed and simulated data, finding the model effectively represented Tmax, Tmin, and Relative Humidity from 1983 to 2014, but had limitations in reproducing historical precipitation. Bias correction using the Delta Method was applied to address underestimation. Statistical methods confirmed the reliability of the generated historical models. For the Local Climate Model (2015-2100), Station 1 and 2 showed similar precipitation changes under SSP2-4.5 and SSP5-8.5 until 2063, after which they diverged. Station 3 experienced significantly higher precipitation changes. Anomalous precipitation under SSP5-8.5 transitioned from negative to positive anomalies around 2049. The impact of SSP5-8.5 on precipitation seemed greater than SSP2-4.5, less influenced by terrain. Spatial analysis showed elevation differences and a correlation between altitude and precipitation, with higher altitudes experiencing increased precipitation.

ACKNOWLEDGEMENTS

APPROVAL SHEET

This thesis entitled "**ASSESSMENT OF FUTURE RAINFALL PATTERNS IN CAMERON HIGHLANDS USING THE STATISTICALLY DOWNSCALED LOCAL CLIMATE MODEL**" was prepared by LIU NI QIAO and submitted as partial fulfillment of the requirements for the degree of Master of Environmental Technology at Universiti Tunku Abdul Rahman.

Approved by:

_____

(Assoc Prof ChM. Ts. Dr. Tan Kok Weng)   Date: 28/12/23

Supervisor

Department of Environmental Engineering

Faculty of Engineering and Green Technology

Universiti Tunku Abdul Rahman

SUBMISSION SHEET

FACULTY OF ENGINEERING AND GREEN TECHNOLOGY
UNIVERSITI TUNKU ABDUL RAHMAN

Date: 28th December 2023

SUBMISSION OF THESIS

It is hereby certified that **LIU NI QIAO** (ID No: **23AGM00482**) has completed this thesis entitled "ASSESSMENT OF FUTURE RAINFALL PATTERNS IN CAMERON HIGHLANDS USING THE STATISTICALLY DOWNSCALED LOCAL CLIMATE MODEL" under the supervision of ChM. Ts. Dr. Tan Kok Weng (Supervisor) from the Department of Environmental Engineering, Faculty of Engineering and Green Technology.

I understand that University will upload softcopy of my thesis in pdf format into UTAR Institutional Repository, which may be made accessible to UTAR community and public.

Yours truly,

Liu Niqiao

(LIU NI QIAO)

DECLARATION

I hereby declare that the thesis is based on my original work except for quotations and citations which have been duly acknowledged. I also declare that it has not been previously or concurrently submitted for any other degree at UTAR or other institutions.

Liu Niqiao

(LIU NI QIAO)

Date   28th December 2023

TABLE OF CONTENTS

LIST OF TABLES

LIST OF FIGURES

Chapter1

Introduction

Anthropogenic activities have been conclusively identified as the primary causal factor for the observed global warming of 1°C (with a range of 0.8–1.2°C) above pre-industrial levels. Projections indicate a further increase to 1.5°C within the timeframe spanning from 2030 to 2052 (IPCC, 2018). The scientific community has accorded significant attention to prospective alterations in climate, particularly with regard to extreme climatic events, due to their potential hazards for societies. Notably, heightened precipitation extremes have a direct bearing on communities as they are closely associated with both flooding and drought occurrences. In addition to recent calamitous events of global scale, such as the Pakistan Floods claiming a minimum of 1,739 lives (June to October 2022), the Floods in Nigeria resulting in a loss of at least 612 lives (June to November 2022), South African Flooding claiming the lives of a minimum of 461 individuals (April 2022), Floods causing a loss of a minimum of 233 lives in Brazil (February 2022), Flooding in India resulting in a minimum of 192 casualties (June to September 2022), and Floods taking more than 182 lives in Afghanistan (August 2022) (USNEWS, 2022). Hence, the prediction of future rainfall pattern is required to take adequate mitigation measures.

The majority of hydrological investigations have primarily relied on ground station data. Precipitation forecasting, particularly in relation to rainfall, poses a significant challenge within the hydrological cycle (Bennett et al., 2013). In most areas, rain gauge stations serve as accessible instruments for estimating precipitation. However, it is noteworthy that limitations, such as inadequate coverage in remote regions or the presence of only one or two rain gauges in expansive catchment areas, are prevalent in developing nations like Malaysia (Norsyuhada et al., 2023). Global Climate Models (GCMs) exemplify numerical models that encapsulate physical processes across the atmosphere, oceans, cryosphere, and land surface. These models stand as advanced tools presently at our disposal for simulating responses within the global climate system. When coupled with nested regional models, simpler models are employed to provide

comprehensive or averaged assessments of climate response. They hold the potential to yield geographically and temporally reliable evaluations of global climate change (Wilby and Dawson, 2013).

1.1 Problem statement

In Cameron Highlands, Pahang, a district recently encountered mud floods, resulting in the inundation of certain areas with knee-deep, sediment-laden water. These inundations were precipitated by a prolonged three-hour downpour that commenced at approximately 3 pm on a Tuesday in Kampung Raja. According to Dilip Martin (2022), the president of Regional Environmental Awareness Cameron Highlands (REACH), this event constitutes the second instance of such mud floods, the initial occurrence transpiring on November 18. The prevailing belief is that an agricultural undertaking established roughly 300 meters uphill from the residential zone may have instigated these mud floods. His report has stated that this undertaking to the residential area, thereby augmenting the potential peril of calamitous events. In light of this situation, it is anticipated that human lives may be imperilled by flooding due to heightened precipitation resulting from the confluence of global warming, soil erosion, and deforestation attributed to the excessive utilization of agricultural land.

1.2 Objectives

1. To develop the local climate model using the statistical downscaling approach.
2. To assess the performance of the statistically downscaled local climate model based on SSP2-4.5 and SSP5-8.5
3. To analyse the changes in rainfall patterns (2015–2100) using spatial analysis.

1.3 Limitations

Limitation 1: Monitoring stations for rainfall, wind, humidity, etc. may be in disrepair and certain nations may not pay attention to the gathering of data from the stations, which may lead to an insufficient collection of historical data and reduce the utility of the climate models.

Limitations 2: Since no data model can ever be completely accurate, when a severe disaster is projected to happen at a specific moment, it is crucial to consider not only the outcome of the prediction but also the findings of a variety of studies, field research, and

previous arguments in order to come to a conclusion. The study will be criticised and lead to conflict between the public, the government, and the research department if the government implements a number of costly and time-consuming steps in response to the forecast, but no catastrophic calamity actually materialises.

Chapter 2

Literature review

2.1 The Global Climate Model (GCM)

Global climate models (GCMs) serve as fundamental tools for investigating water systems (Knutti and Sedla´ˇcek, 2013; Vrac et al., 2007). Nevertheless, their spatial resolution proves inadequate when examining localized effects on various water systems, given the intricacies of local processes (Frías et al., 2006; Xu, 1999). The prevalent approaches employed to address the limitations of coarse resolutions include dynamical downscaling and statistical downscaling methodologies (Vrac et al., 2007).

2.2 Downscaling approach

Downscaling methodologies encompass both statistical and dynamical approaches. Statistical downscaling involves discerning relationships between large-scale climate drivers and local-scale climate conditions. The large-scale climate drivers, as simulated by Global Climate Models (GCMs), serve as predictors in statistical models, facilitating the inference of local climate variables (e.g., analogue downscaling as demonstrated by Pierce et al., 2014; Timbal et al., 2008; Turco et al., 2017). On the other hand, dynamical downscaling employs Regional Climate Models (RCMs) operating at high spatial resolution. These RCMs are driven by boundary conditions derived from the respective GCMs (Giorgi and Gutowski, 2015; Xu et al., 2019).

2.2.1 Dynamical Downscaling

Important hydrological processes, like the effect of antecedent water storage and adherence to the water balance principle, might not be completely captured by statistical models (Humphrey and Gudmundsson, 2019). Furthermore, statistical

downscaling presents difficulties in areas where the relationship between changes in large-scale water storage and local features is not easily apparent (Yin et al., 2018).

As opposed to statistical downscaling, dynamical downscaling uses data assimilation techniques to incorporate target datasets into numerical models in order to produce physically compatible results (Sun et al., 2019). By using global model simulation outputs to feed regional models based on particular physical interactions, dynamic downscaling makes it possible to generate finer resolution data at smaller sizes. According to Fowler et al. (2007), this method is not constrained by data or the strength of the link between local and large-scale factors in any particular place worldwide. Concurrently, the thorough integration of physical processes and parameterization schemes into the regional model guarantees the accuracy of simulation results.

Dynamical downscaling methods find widespread application in investigating both mean and extreme climates in China, owing to their elevated spatial resolution, precise surface parameterization, and intricate parameterization schemes (Guo et al., 2018; Wu et al., 2020).

2.2.2 Statistical Downscaling

Global Climate Models (GCMs) typically feature horizontal resolutions ranging from 250 to 600 km, rendering their outputs unsuitable for accurate local impact studies due to the inherent lack of detailed information required at the local level. Researchers have created tools and techniques for statistical and dynamic downscaling in order to overcome these constraints (Wilby and Dawson, 2013). Wilby and Dawson (2013) conducted a thorough analysis that explores the most popular statistical downscaling techniques, their drawbacks, and problems that may likely arise in the future. Presently, statistical downscaling techniques are considered more cost-effective, flexible, and computationally less demanding compared to dynamic downscaling methods (Wilby and Wigley, 1997; Benestad, 2004).

A primary objective of statistical downscaling studies is to assess the comparative efficacy of statistical versus dynamic approaches, as well as to compare various statistical models. Among the extensively utilized statistical downscaling tools are SDSM and LARS-WG. Over the past decades, numerous studies have employed various statistical downscaling tools to generate future climate change scenarios at local weather stations.

2.2.3 The Comparison of Statistical Downscaling and Dynamical Downscaling

Dynamical downscaling, as exemplified by regional climate models (RCMs), is characterized by computational intensity but offers a physically robust representation of climate dynamics. Despite the advancement introduced by RCMs, their resolution remains coarse, necessitating further downscaling. Consequently, high-resolution models, often referred to as local area models, can be generated by downscaling either an RCM or even a GCM. However, the resource-intensive nature of this procedure, both in terms of computational costs and human resources, limits the availability of downscaled models suitable for local studies. It is advised that climate model ensembles be taken into account in order to account for uncertainties when addressing this restriction (Benestad et al., 2017; Maraun et al., 2010). As a result, the limited number of models available may raise questions about how reliable local studies using dynamical downscaling are.

In contrast, statistical downscaling offers a relatively straightforward process for producing large climate model ensembles. This approach seeks to establish relationships between large-scale variables and local observations, with the advantage of lower computational costs. Noteworthy is the fact that RCMs provide a more nuanced understanding of processes at the regional scale (Maraun et al., 2010). Therefore, it is considered best practice to employ both statistical and dynamical downscaling methods synergistically: (i) for downscaling an RCM to a local scale and (ii) to rectify biases in high-resolution models.

2.3 Statistical downscaling approach

2.3.1 Linear regression

Using linear regression analysis, one can forecast a variable's value depending on the value of another variable. The variable that you wish to be able to forecast is the dependent variable. The variable you are using to forecast the value of the other variable is known as the independent variable.

Simple linear regression is an empirical method for addressing problems in the statistical sense that takes into account the historical data set of climatic values or parameters. There can only be one dependent variable and one independent variable in it. There can only be two variables in a basic linear regression model. Simple linear regression will be depicted as follows:

$$Y = \alpha + \beta X$$

where Y is the dependent variable, X is the independent variable, and, are the regression coefficients. We shall execute simple linear regression by calculating the slope and intercept since it will resemble a mathematical equation of slope and intercept line. The strength and direction of the association between the two variables can be determined using the regression coefficient formula. The mathematical and statistical evolution processes may also be used to calculate various correlation coefficient formulae. The formula for r is as follows:

$$Y = \frac{\Sigma(x_i - \bar{x})(y_i - \bar{y})}{\Sigma(x_i - \bar{x})^2}$$

The ability of the regression line to represent the data is measured by the coefficient determination. One can characterize the degree and direction of the relationship between the independent and dependent variables. The difference between the actual and expected values, as well as the error, can be calculated after calculating the projected values. The method for figuring out mistake is

$$RMSE = \sqrt{\frac{(y_i - \bar{y_l})^2}{n}}$$

Yi = Actual value, $\bar{y_l}$ = Predicted value, n = Total number of samples. RMSE can be known as root mean square error or root mean square deviation. It can be used measure of difference between sample and population value.

2.3.2correction test

When compared to local climate variables for a reference period, the raw GCM climate predictors are typically prone to biases in the magnitude and frequency of a climate variable. As previously stated, this is true especially with precipitation. In light of these shortcomings, a brand-new class of statistical downscaling techniques known as QM bias-correction techniques have been put out recently, and they seem to be more effective at forecasting local climate than the traditional SDSM.

Quantifying potential biases by contrasting the distribution of the GCM-simulated climate predictors with that of the regionally observed variables over the historical reference period forms the fundamental premise of all bias-correction techniques. Furthermore, the primary premise in the application of classical QM is the stationarity of the biases and other distributional properties, such as variance and skewness, meaning that these parameters—aside from the distribution's mean, which is subject to change—should remain constant for both the reference and subsequent periods.

Non-stationary QM bias-correction techniques have recently been proposed, which have been shown to be more effective tools for decreasing the bias of GCM predictors than the earlier stationary QM methods. There is now sufficient evidence to show that the statistics of the climate variables will not necessarily be stationary.

2.4 Shared Socioeconomic Pathways (SSPs)

Shared Socioeconomic Pathways (SSPs) are projections of anticipated worldwide socioeconomic trends through the year 2100. They are applied to create scenarios for greenhouse gas emissions under various climate policies. The most recent climate models currently incorporate these SSPs as significant inputs, which will be included in the IPCC's sixth assessment report, which is scheduled for publication in 2020–21. They are also being used to investigate how societal decisions may impact greenhouse gas emissions and, consequently, how the Paris Agreement's climate goals might be achieved.

According to the SSP2-4.5 and SSP5-8.5 scenarios, Chen et al. (2023) analyses the changes in wind power and related CAP caused by climate change across China in the two-level years (2030 and 2060). The findings indicate that in 2060, the wind capacity factor over China will be on a downward trend in most parts of the country and

upward in the southeast. In general, climate change will have a minimal effect on the CAP of wind power in 2030, however some southern areas would experience a rise.

The Shared Socioeconomic Pathway scenarios (SSPs) of the CMIP6 used six distinct Regional Climate Models, which were bias-corrected with CMhyd across Greater Accra utilising ground station and PUGMF reanalysis data. (Ebenezer et al). According to the study, the intensity of precipitation in the area covered by the SSPs has decreased and may have even shifted. Under the SSP1-2.6, SSP2-4.5, SSP3-7.0, and SSP5-8.5 scenarios, respectively, maximum temperatures are predicted to rise by 0.81-1.45°C, 0.84-1.54°C, 0.96-1.70°C, and 0.98-1.73°C, while minimum temperatures are predicted to rise by 1.33-2.02°C, 1.49-2.22°C, 1.71-4.75°C, and 1.75-4.83°C.

Under shared socioeconomic pathway and representative concentration pathway (SSP-RCP) scenarios, combining land use and climate change can produce more precise projections of the risks to water supply, assisting decision-making for spatial planning with an emphasis on climate adaptation. There are both temporal and regional variations in climate change. Further study is required to evaluate the hazards associated with the water supply at various basin or regional sizes in order to satisfy the needs of spatial planning. In order to analyse four SSP-RCP scenarios, Tang et al. (2023) took the temporal scale of spatial planning into account. Using a Taylor diagram, which rates the effectiveness of climate element simulations, five global climate models (GCMs) and a multi-model ensemble (MME) were assessed for their ability to simulate climate.

Chapter 3

Methodology

3.1 Research Study Set-up

The Study workflow of this study showed in Figure 3.1
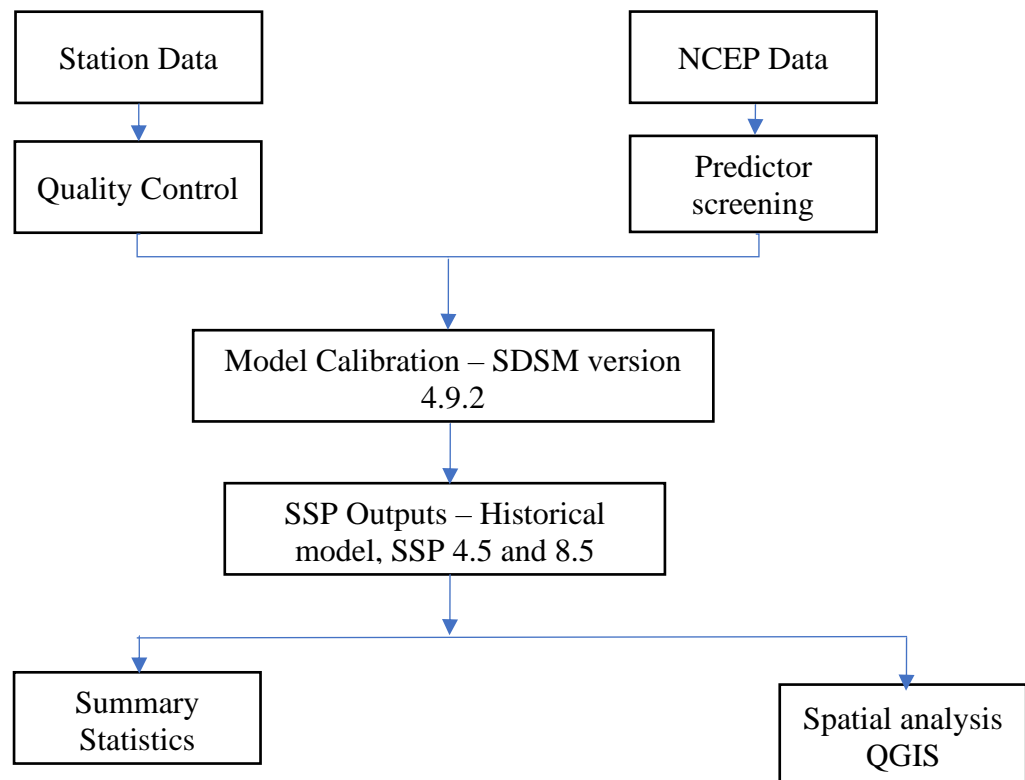
Figure 3.1: The Study Workflow

3.2 Study Area

Cameron Highlands, situated in the state of Pahang, exhibits diverse terrain with elevations ranging from 1070 to 2110 meters above sea level. Characterized by its mountainous topography, it stands as the smallest district in Pahang, occupying the

Northwestern corner of the state over a total area of 71,000 hectares and hosting a population of around 300,000 residents. Sharing borders with the states of Kelantan to the north and Perak to the west, Cameron Highlands is comprised of three mukims: Mukim Ulu Telom, Mukim Ringlet, and Mukim Tanah Rata. These mukims collectively encompass nine places, including Blue Valley, Kg. Raja, Kuala Terla, Tringkap, Kea Farm, Tanah Rata, Brinchang, Ringlet, and Kg. Bertam Valley.

Presently, a significant portion of Cameron Highlands, amounting to 5890 hectares, is dedicated to agricultural activities, primarily focused on vegetable farming. Meteorological data indicates that the region receives an average annual rainfall of approximately 2800 mm.

3.3 Data

3.3.1 Observed climate data

Daily precipitation (Prcp), maximum temperature (Tmax), minimum temperature (Tmin), and humidity data were gathered from both the NASA Earthdata portal and the Malaysia Meteorological Department (MMD). This dataset covers the period from 1983 to 2022 and pertains to three specific stations located in the Cameron Highlands of Malaysia (refer as figure 3.2). To ensure data integrity, the SDSM 4.2 software's quality control function was employed. Addressing weather data quality is a critical undertaking in developing nations due to the prevalent occurrence of missing data. Failing to rectify these gaps can impede subsequent processes such as predictor screening and calibration. In the context of this study, station one exhibited 12 instances of missing data. These gaps were distributed such that every three missing data points were observed in the daily Prcp, Tmax, Tmin, and humidity variables within the dataset obtained from the NASA Earthdata portal (https://power.larc.nasa.gov/). As emphasized by Wilby et al. (2014), regions most susceptible to climate variability often coincide with those exhibiting substantial data deficiencies.
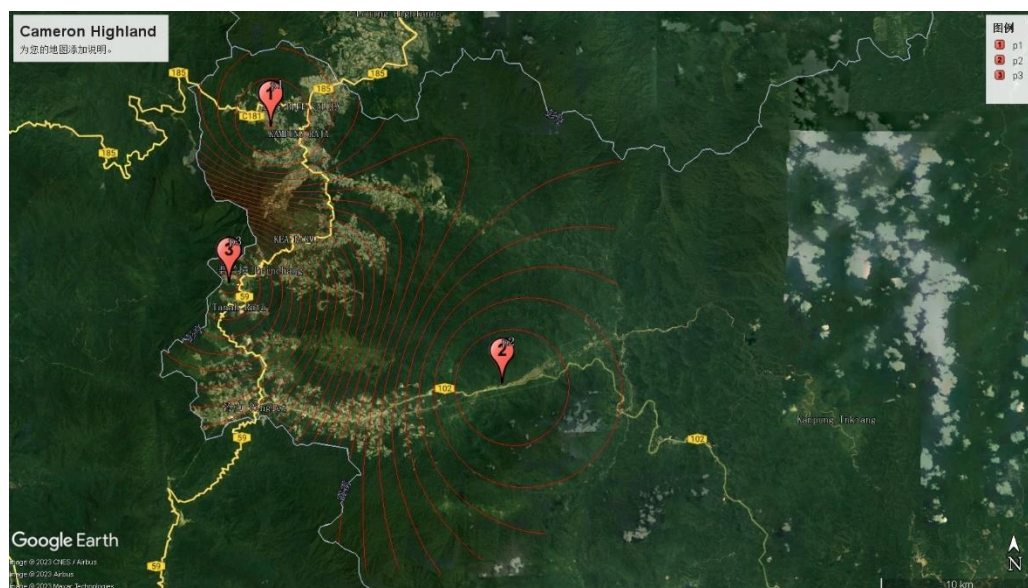
Figure 3.2: The Location of three Station

3.3.2 GCMs used NECP data and Predictor Screening

The investigation made use of the The Canadian Earth System Model version 5 (CanESM5)a Global Climate Model (GCM). Notably, CanESM5 demonstrates a higher equilibrium climate sensitivity of 5.6 $^{\circ}$K in comparison to its precursor, CanESM2, which registered 4.5 $^{\circ}$K. Predictors refer to large-scale variables housed within the archives of the GCMs.

Predictors should, in an ideal situation, be conceptually and physically coherent with their matching predictands, or the observed data. Furthermore, accurate modeling by the GCMs depends on a strong and stable connection between predictors and predictands. Preference was given to the set of predictors that included circulation, stability, thickness, and moisture content factors in order to downscale precipitation. As Siabi et al. (2021) point out, these predictors are crucial to the model's calibration and validation.

A total of 26 predictors, as detailed in Table 3.1, sourced from the National Centres for Environmental Prediction (NCEP) and National Centre for Atmospheric Research (NCAR) reanalysis dataset of CanESM5, were utilized for model calibration. All three stations were accommodated within a unified GCM framework for the downscaling process. Consequently, CanESM5 and NCEP data were employed for

model calibration, whereas CanESM5 predictors were utilized for both model validation and generating future projections. Notably, the predictors derived from CanESM5 are available under the SSP2-4.5 and SSP5-8.5 scenarios for future climate projection downscaling, spanning from 2015 to 2100.

Table 3.1: The 26 atmospheric predictors

No.	Variable ID	Predictor variable
1	mslp	Mean sea level pressure
2	p1_f	1000 hPa Wind speed
3	p1_u	1000 hPa Zonal wind component
4	p1_v	1000 hPa Meridional wind component
5	p1_z	1000 hPa Relative vorticity of true wind
6	p1th	1000 hPa Wind direction
7	p1zh	1000 hPa Divergence of true wind
8	p5_f	500 hPa Wind speed
9	p5_u	500 hPa Zonal wind component
10	p5_v	500 hPa Meridional wind component
11	p5_z	500 hPa Relative vorticity of true wind
12	p5th	500 hPa Wind direction
13	p5zh	500 hPa Divergence of true wind
14	p8_f	850 hPa Wind speed
15	p8_u	850 hPa Zonal wind component
16	p8_v	850 hPa Meridional wind component
17	p8_z	850 hPa Relative vorticity of true wind
18	p8th	850 hPa Wind direction
19	p8zh	850 hPa Divergence of true wind
20	p500	500 hPa Geopotential
21	p850	850 hPa Geopotential
22	prcp	Total precipitation
23	s500	500 hPa Specific humidity
24	s850	850 hPa Specific humidity
25	shum	1000 hPa Specific humidity
26	temp	Air temperature at 2m

3.4 SDSM (Statistical Downscaling Model)

The SDSM uses a hybrid methodology that combines multiple linear regression with a stochastic weather generator. The latter provides an empirical link between data from the National Centers for Environmental Prediction (NCEP) and variables from the Global Climate Model (GCM). By using a multilinear regression model and stochastic bias-correction approaches, SDSM establishes a statistical relationship between the

GCM variables (predictors) and the local variables (predictands), facilitating the downscaling of GCM outputs.

Subsequent to data quality control procedures, predictors were selected for each predictand based on criteria such as correlation, partial correlation, and P-value matrices. This selection process was carried out using the Statistical Package for the Social Sciences (SPSS) software. Typically, more than 78 iterations (3 stations $\times$ 26 predictors) were analysed for a single predictand, and 312 iterations (3 stations $\times$ 26 predictors $\times$ 4 predictands) were conducted for the four predictands (precipitation, Tmax, Tmin, and Humidity) employed in this study. The model was implemented at a monthly temporal scale to enhance its performance. Additionally, in configuring SDSM for calibration, two distinct datasets were requisitioned: daily observed data and NCEP daily predictors. The model was calibrated using selected predictors for each predictand, a process executed through rigorous screening. Temperature and humidity variables (Tmin, Tmax, and Humidity) were calibrated under unconditional processes at a monthly scale, whereas precipitation underwent calibration under conditional processes, also on a monthly scale.

The model, when calibrated with the most strongly correlated predictors, generated up to 100 ensembles of daily time-series data, with the ensemble mean serving as its corresponding output. However, for the purposes of this study, the model's output comprised 20 ensembles for the current period. The ensemble mean was employed to assess the performance of SDSM in simulating local data (Wilby and Dawson, 2007; Tavakol-Davani et al., 2013).

3.4.2 QGIS (Quantum Geographic Information System)

A free, open-source programme called QGIS (Quantum Geographic Information System) enables users to generate, modify, visualise, analyse, and publish geographic data. To generate spatial analysis of annual rainfall averages for Cameron Highland under the SSP2-4.5 and SSP5-8.5 scenarios, the following steps were undertaken. Firstly, the "open street map" function was employed to pinpoint the specific place of Cameron Highland. Subsequently, a new shape line layer was created to delineate the boundaries of Cameron Highland. It is imperative to note that the conversion of the multiline layer to a polygon layer using the geometry tool was necessary in order to enable the application of the "clip raster by mask layer" function.

Secondly, a delimited text layer was added to input the files (refer to table 3.2 and 3.3). p1, p2, and p3, represent the three designated research places, along with their respective longitude and latitude coordinates, allowing for precise identification on the polygon layer map. Additionally, the numerical ranges 15-35, 36-55, 56-75, and 76-100, in conjunction with their corresponding lists, respectively denote aggregated annual precipitation for the years 2015 to 2035, 2036 to 2055, 2056 to 2075, and 2076 to 2100. Thirdly, the IDW interpolation function was employed to analyse precipitation for each of the four time periods on the polygon layer, with fixed pixel coordinates of x and y at 0.0001, resulting in the production of eight distinct maps. Subsequently, the "clip raster by mask layer" function was applied to remove any excess areas outside the boundaries of Cameron Highland.

Finally, adjustments were made to the properties of the eight clipped maps. Specifically, the render type was modified to "singleband pseudocolor," and the minimum and maximum precipitation values were standardized. The interpolation method was set to discrete, with the mode fixed at quantile and 7 quantile value range. Notably, it is crucial to ensure that the quantile value ranges and the colour ramp across all eight maps are consistent, in order to facilitate clear visualization of rainfall variations.

Table 3.2: Average Annual precipitation (2015-2035, 2036-2055, 2056-2075, 2076-2100) of three places based on SSP2

ID	longitude	latitude	15-35	36-55	56-75	76-100
p1	101.394	4.5714	2499.7	2602.8	2689.6	2777.9
p2	101.5229	4.428	2479.7	2579.5	2675.9	2760.8
p3	101.3714	4.4842	3052.8	3179.2	3268.7	3379.9

Table 3.3: Average Annual precipitation (2015-2035, 2036-2055, 2056-2075, 2076-2100) of three places based on SSP5

ID	longitude	latitude	15-35	36-55	56-75	76-100
p1	101.394	4.5714	2495.3	2688.0	2865.9	3128.6
p2	101.5229	4.428	2503.1	2663.4	2850.7	3079.2
p3	101.3714	4.4842	3031.4	3367.2	3499.7	3606.5

Chapter 4

Results and Discussion

4.1 Historical Model Generation

4.1.1 Precipitation

The observational data encompassing daily precipitation, daily maximum and minimum temperatures, as well as daily humidity, spanning from January 1, 1983, to December 31, 2022, were acquired from two distinct geographical coordinates using NASA's POWER dataset. Station 1 is situated at a latitude of 4.5714 and a longitude of 101.394, while Station 2 is positioned at a latitude of 4.4663 and a longitude of 101.5836.

The historical models for both Station 1 and Station 2 were constructed utilizing the SDSM software within the temporal range of 1983 to 2014. These models were subsequently juxtaposed with their respective sets of observational data. As depicted in Figures 4.1 to 4.5, owing to the proximity of the two places, the generated historical models exhibit notable similarity, with the observational data displaying a corresponding degree of comparability. One can argue that the climate in Cameron highland does not vary substantially spatially because of its small area. Notably, with regard to the annual mean precipitation (refer to figure 4.1 and 4.2), both generated historical models exhibited a tendency to overestimate the corresponding observational data (red curve displays historical observed data, green curve demonstrates the modelled data). However, for maximum precipitation values (refer to figure 4.3 and 4.4), the historical models demonstrated a proclivity to underestimate the actual observed data; in other words, the historical model cannot predict the extremely change of maximum precipitation.
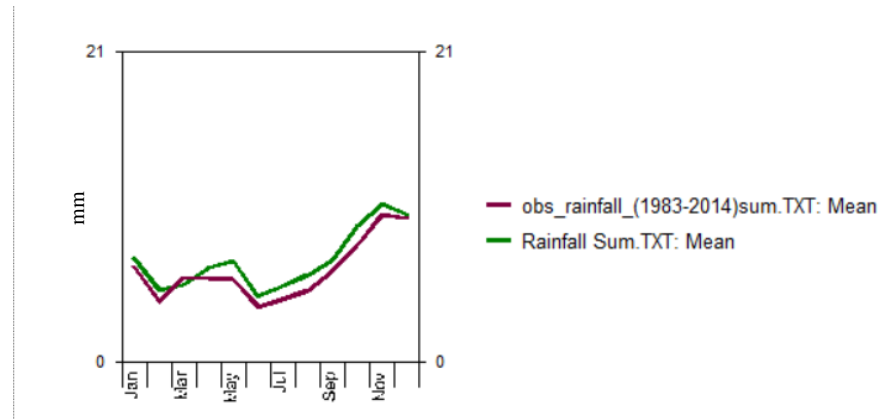
Figure 4.1: Mean of Average Monthly Rainfall of Station 1
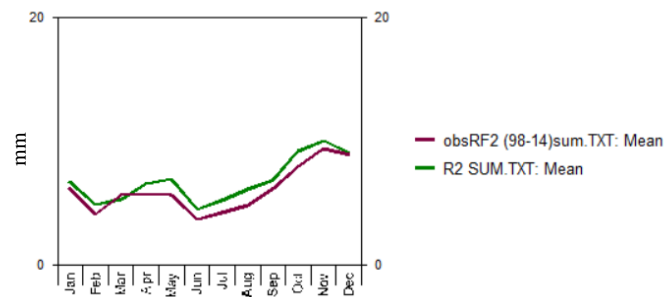
Figure 4.2: Mean of Average Monthly Rainfall of Station 2
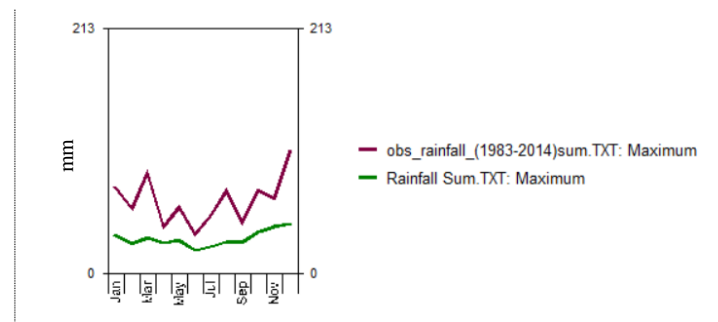
Figure 4.3: Maximum of Average Monthly Rainfall of Station1
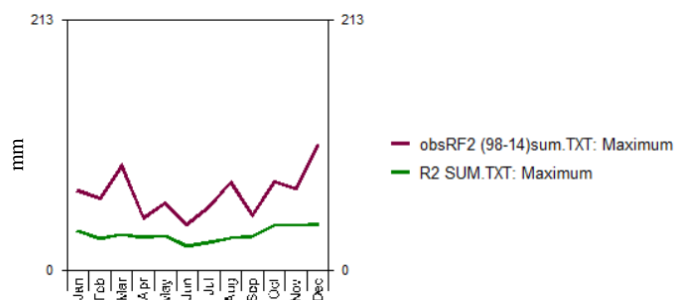
Figure 4.4: Maximum of Average Monthly Rainfall of Station2
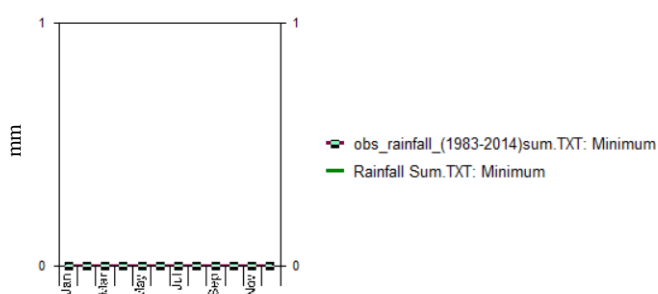
Figure 4.5: Minimum of Average Monthly Rainfall of Station1
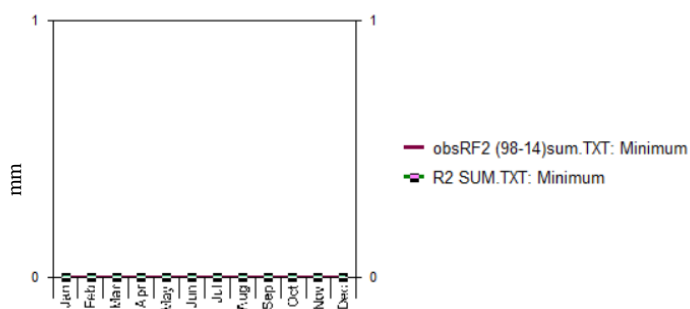
Figure 4.6: Minimum of Average Monthly precipitation of Station 2

4.1.2 Temperature Maximum

The outcomes of juxtaposing the historical predictive models with actual maximum temperature observations at the specified places, depicted in Figures 4.7 to 4.12, manifest that the historical models demonstrated a commendable level of accuracy in forecasting

observed values. While occasional instances of both overestimation and underestimation of observed data were noted (refer to Figure 4.9 and 4.10), the graphs (refer to Figure 4.7 and 4.8) illustrating the average maximum temperatures at both places exhibited a seamless alignment, thereby diminishing the significance of these disparities to a negligible extent.
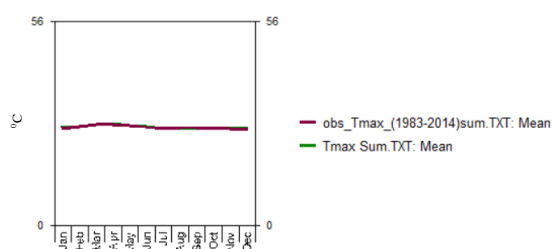
Figure 4.7: Mean of Average Monthly Maximum Temperature of Station1
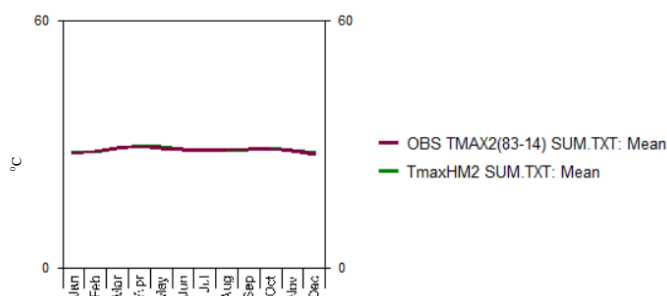
Figure 4.8: Mean of Average Monthly Maximum Temperature of Station2
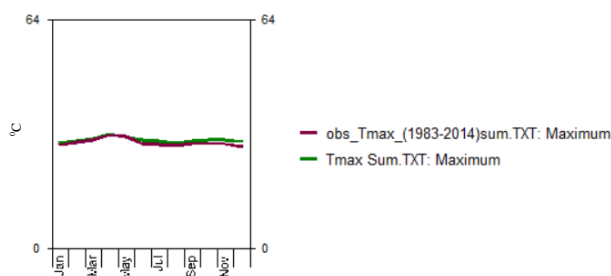
Figure 4.9: Maximum of Average Monthly Maximum Temperature of Station 1
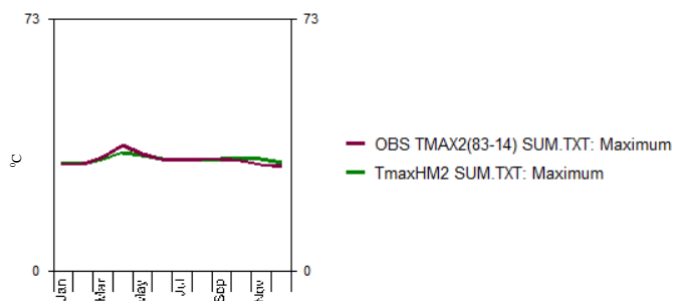
Figure 4.10: Maximum of Average Monthly Maximum Temperature of Station2
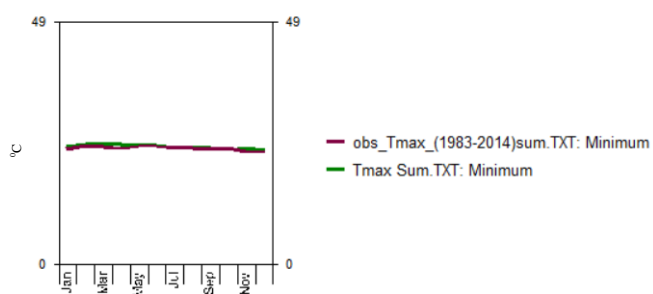
Figure 4.11: Minimum of Average Monthly Maximum Temperature   of Station 1
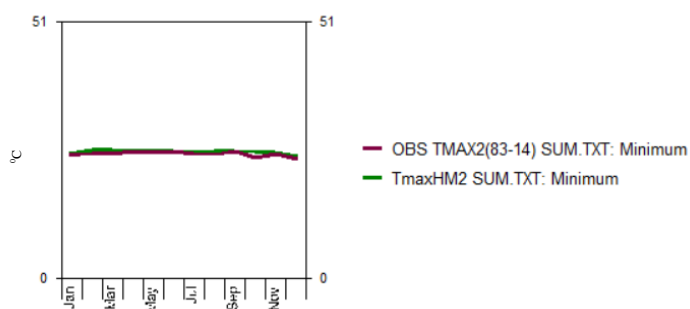
Figure 4.12: Minimum of Average Monthly Maximum Temperature of Station2

4.1.3 Temperature Minimum

The outcomes of evaluating the historical predictive model against the actual maximum temperature observations at a specific site are presented in Figures 4.13 to 4.18. These figures illustrate that the historical model demonstrates noteworthy precision in forecasting the observations. Similarly, the graph representing the average minimum temperature at two distinct stations(refer to Figure 4.13 and 4.14) showcases a coherent correlation, thereby diminishing the magnitude of these disparities to negligible proportions.
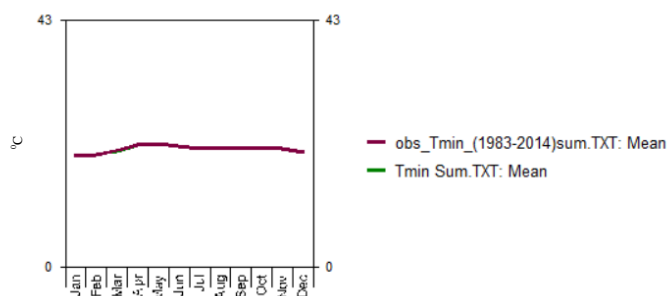
Figure 4.13: Mean of Average Monthly Minimum Temperature of Station1
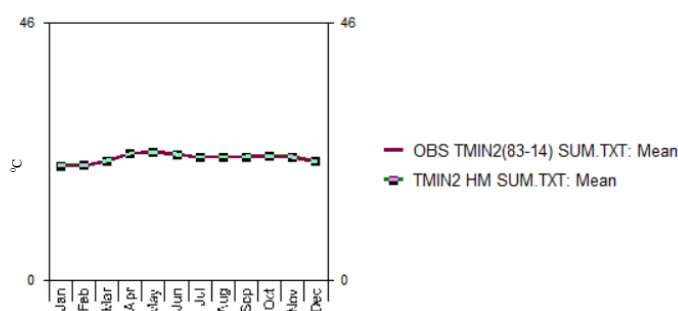
Figure 4.14: Mean of Average Monthly Minimum Temperature of Station2
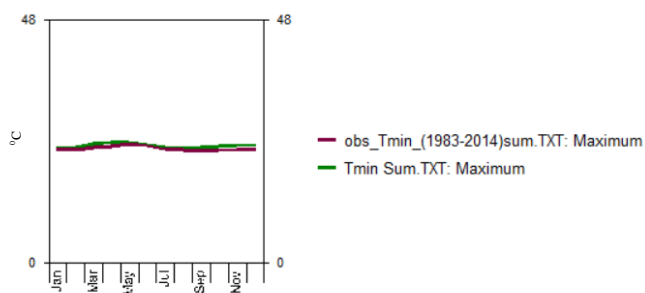
Figure 4.15: Maximum of Average Monthly Minimum Temperature of Station 1
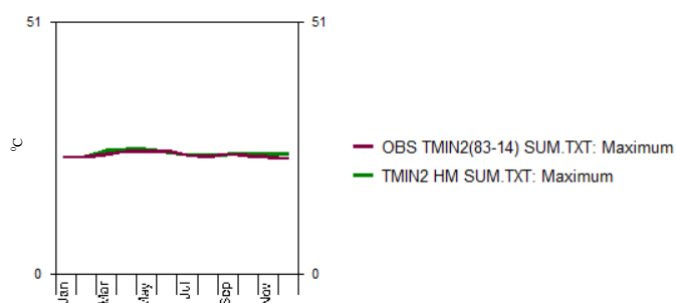
Figure 4.16: Maximum of Average Monthly Minimum Temperature of Station 2
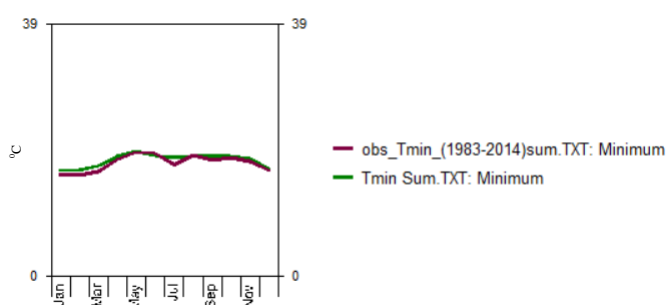
Figure 4.17: Minimum of Average Monthly Minimum Temperature   of Station1
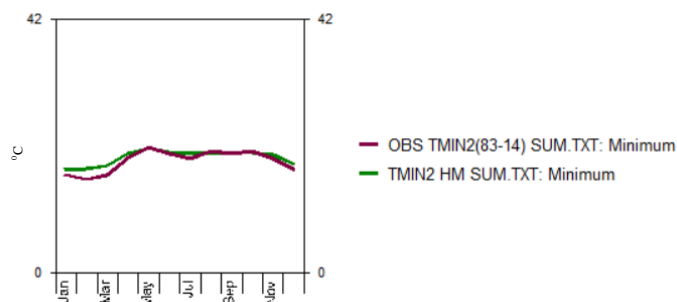
Figure 4.18: Minimum of Average Monthly Temperature minimum of Station 2

4.1.4 Relative Humidity

As indicated by Figures 4.23 and 4.24, it becomes evident that the historical model exhibits a limited sensitivity to pronounced variations and tends to overestimate the observed values, From June to August, the historical observed humidity percentage deviates from simulated values by initially decreasing and then subsequently increasing, eventually realigning with the simulated humidity. The minimum humidity occurs in July (refer to Figures 4.23). Meanwhile (refer to Figures 4.24), There were two instances of observed humidity dropping and then rising again, with the current occurrence having a larger span. This pattern was observed from March to June and from June to September. The historical minimum humidity percentage was recorded in April. This phenomenon could potentially be attributed to the intricate nature of the local meteorological processes, rendering them challenging to simulate comprehensively, thereby impeding the model's capacity for accurate representation. Moreover, protracted climatic trends and unforeseen meteorological events may contribute to instances of overestimation in observational data.
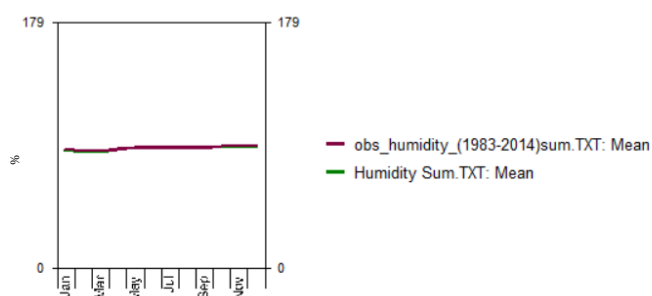
Figure 4.19: Mean of Average Monthly Relative Humidity of Station 1
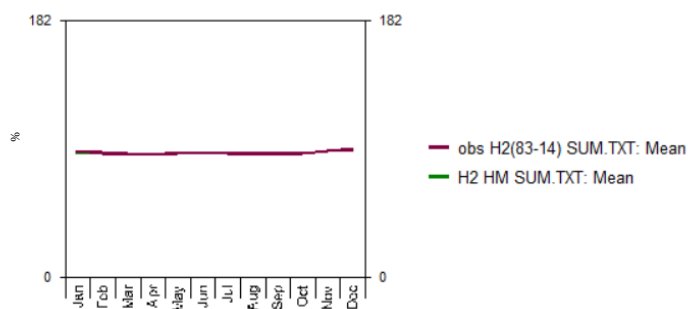
Figure 4.20: Mean of Average Monthly Relative Humidity of Station 2
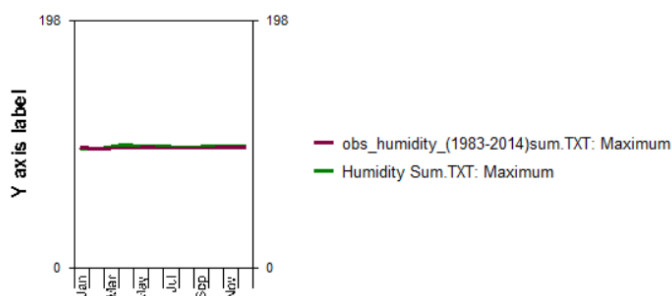
Figure 4.21: Maximum of Average Monthly Relative Humidity of Station 1
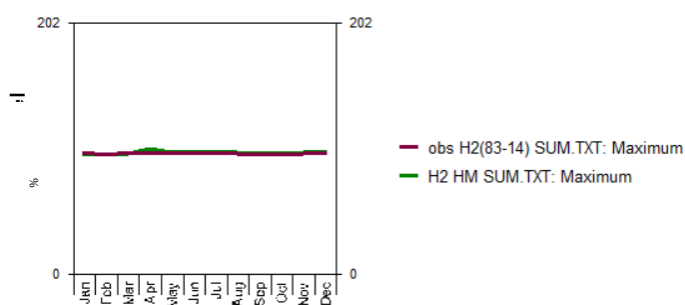
Figure 4.22: Maximum of Average Monthly Relative Humidity of Station 2
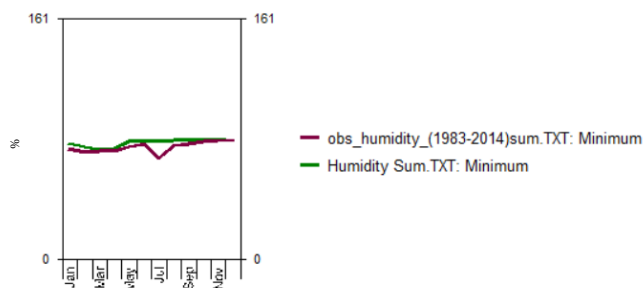
Figure 4.23: Minimum of Average Monthly Humidity of Station 1
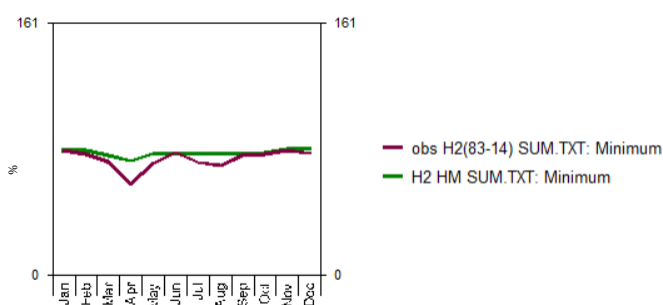
Figure 4.24: Minimum of Average Monthly Relative Humidity of   Station 2

Based on the aforementioned figures, it is evident that Cameron Highlands in Malaysia experiences pronounced fluctuations in rainfall, while exhibiting minimal deviations in temperature and humidity. Specifically, parameters such as temperature maximum, temperature minimum, and humidity, particularly their mean values, demonstrate a consistent horizontal trajectory over the course of a year. This apparent lack of correlation between precipitation and variables such as Tmax, Tmin, and humidity can be attributed to two primary factors. Firstly, Cameron Highlands is distinguished by its rugged topography, characterized by elevated terrain. When moist air originating from adjacent areas encounters these elevated features, it undergoes forced ascent, inducing orographic lifting. Consequently, as the air ascends, it undergoes cooling and condensation, resulting in escalated precipitation levels, particularly in localized regions characterized by significantly heightened rainfall. Secondly, anthropogenic activities, encompassing urbanization, deforestation, and alterations in land use, possess the capacity to influence local climatic patterns. These alterations may, on occasion, lead to adjustments in precipitation regimes.

4.2 Historical model validation using PDF, Prediction Accuracy, Index of Accuracy, RMSE analysis, ANOVA

PDF (Probability Density function): The possibility that a certain outcome will come about from a process that produces observable data is described in (PDF). Using PDFs to determine which values are most likely to occur as well as which values are less likely. Sort the data using the Probability Density function from lowest to highest, where $Z = \frac{X_i - X_{mean}}{\sigma}$; σ = Standard Deviation

PA (Prediction Accuracy):0<x<1

$$PA = \sum_{i=1}^{n} \frac{(P_i - \bar{P})(O_i - \bar{O})}{(n-1)\sigma_p \sigma_o}$$

IA (Index of accuracy):0<x<1

$$IA = 1 - \frac{\sum_{i=1}^{n}(P_i - O_i)^2}{\sum_{i=1}^{n}(|P_i - \bar{O}| + |O_i - \bar{O}|)^2}$$

RMSE (Root mean square error):$(0, \infty)$

to calculate the typical discrepancy between the projected values of a statistical model and the actual values.

$$RMSE = \sqrt{\frac{\sum_{i=1}^{n}(P_i - O_i)^2}{n-1}}$$

ANOVA (Analysis of Variance):

to determine if the two groups' average means vary or not.

- Hypothesis null: There is no statistically significant difference between the means. H0 : $\mu_1 = \mu_2 = \mu_3 \dots$

- Hypothesis one: Some of the mean differences are statistically significant H1 :$\mu_1 \neq \mu_2 \neq \mu_3 \dots$

P ≥ 0.05 rejects H1; accepts H0; F crucial > F value

4.2.1 Precipitation (mm/month)

Output (Station 1):
(In Figure 4.25) Probability density functions (PDFs) serve as a statistical tool for assessing the agreement between the historical model and the observational dataset. The x-axis denotes the precipitation variable, while the y-axis represents the probability density. The blue curve corresponds to the PDF derived from the monthly observation

dataset spanning from 1983 to 2014, while the orange curve depicts the PDF generated by the historical model which from the monthly data of mean of 20 ensembles. Notably, it is discernible that the peaks of the two PDFs do not align, indicating a substantial disparity between the model and the observed data. This lack of convergence in the peak regions suggests that the model may not comprehensively capture specific facets of the observed phenomenon. Moreover, metrics such as PA: 0.635, IA: 0.742, R^2: 0.4035, RMSE (Root Mean Square Error): 73.03, and ANOVA (Analysis of Variance) with a significance level of $P<0.05$ further underscore the model's lack of reliability. Consequently, it is imperative to employ bias correction techniques to refine the model's calibration.
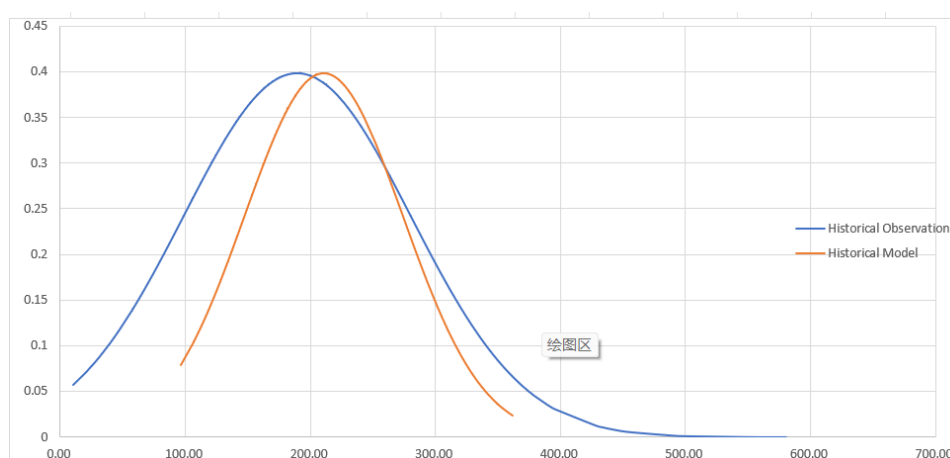
Figure 4.25: Precipitation PDF output of Station 1

For a more comprehensive visual analysis of the Probability Density Functions (PDFs), the Kernel Density Estimation function in the R programming language was employed (see Figure 4.26). This function facilitated an examination of the historical model dataset alongside the observed dataset, yielding the KDE figure (depicted in Figure 4.27). Along the x-axis, the variable of interest, precipitation, is ranged from 0 to 600 mm/monthly, while the y-axis represents estimated density, spanning from 0 to 0.007.

Evidently, discernible peaks in the KDE curves for both the modelled and observed data are observed, manifesting around 200mm/monthly and 150mm/monthly, respectively. Correspondingly, valleys, indicative of lower density regions in the modelled data, are notably situated at approximately

250mm/monthly. Overlapping segments in the KDE curves suggest similarity within the precipitation range of 150 to 350mm/monthly. Noteworthy is the discernible difference in curve width; the historical model dataset exhibits a range from 50 to 400 mm/monthly, while the observed data spans from 0 to 600 mm/monthly. Nevertheless, the slender right tail of the observed data suggests a lower probability, rendering its influence negligible.

It is imperative to highlight the presence of multiple peaks in the KDE curve of the historical model. This phenomenon may arise from two plausible explanations. Firstly, the historical model might incorporate additional variables, features, or factors not accounted for in the observation dataset, leading to the emergence of distinct modes in the KDE. Alternatively, the observation dataset may lack crucial variables or details considered in the historical model, potentially resulting in a simpler, unimodal distribution.

```r
density_data1 <- density(modeled_data$hismodel)
density_data2 <- density(observed_data$obs)
plot(density_data1, main="Kernel Density Estimation", col="blue", lwd=2, xlim=c(min(modeled_data$hismodel, observed_data$obs), max(modeled_data$hismodel, observed_data$obs)))
lines(density_data2, col="red", lwd=2)
legend("topright", legend=c("modeled_data$hismodel", "observed_data$obs"), col=c("blue", "red"), lty=1, cex=0.8)
```

Figure 4.26: The programming coding to obtain the Kernel Density Estimation (KDE)output through the R programming language
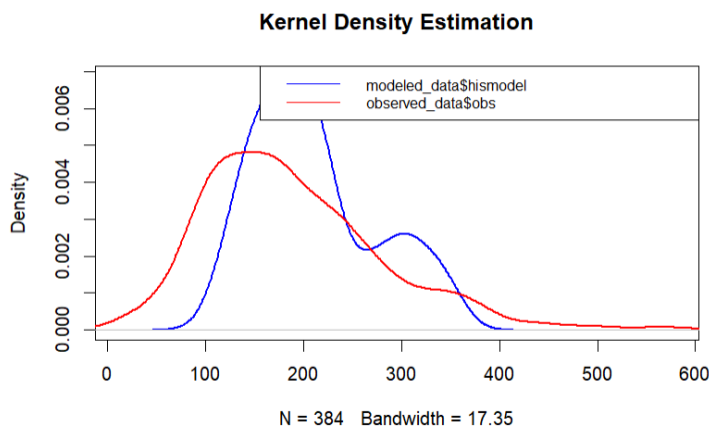
Figure 4.27: TheKernel Density Estimation (KDE)output ofthe historical observed datavs. historical modelled data of Station 1 by R programming language output

Nevertheless, this method (KDE analysis) serves as an initial visual tool for comparing the probability density functions of two datasets. For a more rigorous quantitative assessment of the disparities between the modelled and observed datasets, the Hellinger distance was employed. The Hellinger distance is a statistical metric utilized to quantify the degree of similarity or dissimilarity between two discrete probability distributions, such as probability density functions (PDFs) or histograms. This calculation was executed using the R programming language, yielding an output of 0.244 (refer to Figure 4.28 & 4.29). A Hellinger distance falling within the range of 0 to 0.5 implies a state of moderate to high dissimilarity. Within this interval, the distributions exhibit some degree of overlap but also notable disparities in their shapes.

```
1  modeled_data <- read_excel("C:/Users/HUAWEI/Desktop/model.xlsx",sheet="ModeledData")
2  observed_data <- read_excel("C:/Users/HUAWEI/Desktop/observed.xlsx",sheet="ObservedData")
3  density_data1 <- density(modeled_data$hismodel)
4  density_data2 <- density(observed_data$obs)
5  hellinger_distance <- sqrt(1 - sum(sqrt(density_data1$y * density_data2$y)))
```

```
hellinger_di… 0.244131257481822
```

Figure 4.28 & 4.29: the detailed programming content to get the Hellinger distance value through the R programming language and the corresponding Hellinger distance value

Output after Bias correction:

Delta Method (Precipitation)

$$P_i = P_{sim.i} \times \alpha$$
$$\alpha = P_{ave\ obs}/P_{ave\ sim}$$

where, Pave obs = Average observation value; Pave sim. = Average modelled value; Pi = corrected modelled value at time i; P sim. i = modelled value at time i

After applied the delta method fto bias correct the historical modelled dataset, the PA value doesn't change, IA change from 0.742 to 0.745, R^2 doesn't change 0.4035, RMSE change from to 73.03to 70.2, ANOVA:P>0.05.(refer to Figure 4.30) It illustrates the Probability Density Functions (PDFs) of the bias-corrected historical modelled dataset and the observed data. Notably, there is a noticeable degree of overlap between the two curves, indicating a significant similarity in the underlying distributions. This suggests that the historical model accurately captures certain aspects of the observed phenomenon.
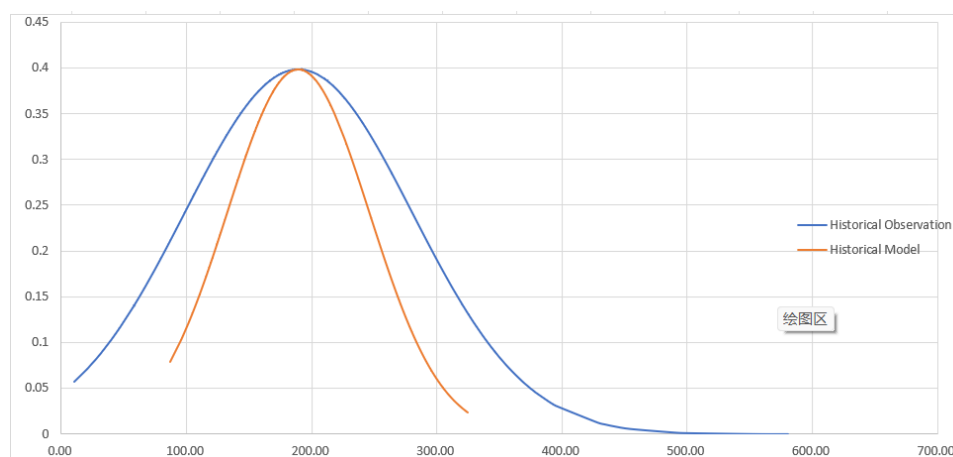
Figure 4.30: Precipitation PDF output of   Station1(Afterbiased correction)

In the biased-corrected KDE (as figure 4.31), the density of peak from 0.007 to 0.006. After bias correction, the Hellinger distance from 0.24 to 0.09 (as figure 4.32), If the Hellinger distance is close to 0, it implies a high degree of similarity between the compared distributions. This suggests that the distributions are very similar in shape, and their overlap is substantial.

Kernel Density Estimation

N = 384   Bandwidth = 15.58
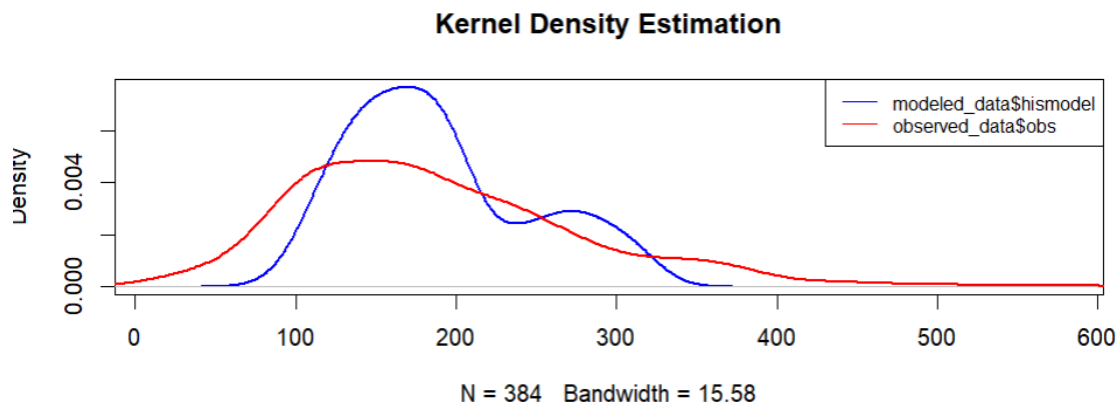
Figure 4.31: the kernel density estimation chart about the historical observed data versus historical modelled data of   Station1 by R programming language output —biased corrected version

hellinger_di… 0.0873288570413902

Figure 4.32: The Hellinger distance value of R programming language output—biased corrected version

Output (Station 2):

Using the duplicated method to analyse the Station 2, the initial result display that PA: 0.605, IA: 0.710, R^2 (coefficient of determination): 0.367, RMSE: 71.6, ANOVA: P<0.05. After using the delta method: PA:0.619, IA: 0.710, R2: 0.383, RMSE: 67.9, ANOVA: P=0.99>0.05, those statistical data substantiate the indistinguishability between the model and observed data in terms of their underlying distributions.
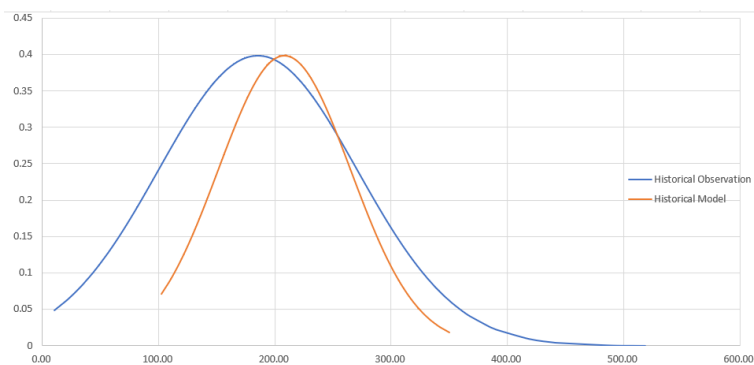
Figure 4.33: Precipitation PDF output of Station2
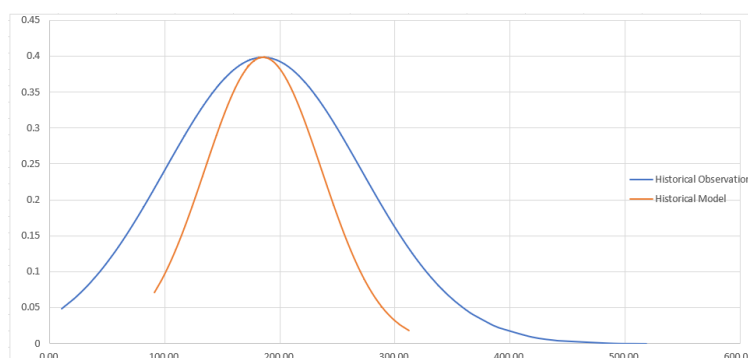
Figure 4.34: Precipitation PDF output of Station2 (Afterbiased correction)

4.2.2 Temperature at 2 Meters Maximum (Tmax) (^{0}C)

Figures 4.35 and 4.36 present the Probability Density Functions (PDFs) depicting the historical model data alongside the historical observation data. Noteworthy is the remarkable correspondence between the two curves, indicating a notable congruence in the underlying distributions. The x-axis delineates the maximum temperature variable, ranging from 25℃ to 30℃, while the y-axis represents the probability density, with its maximum value capped at 0.4. Beyond the evident visual overlap in PDFs, quantitative metrics further affirm this congruence. Specifically, PA at 0.569 and 0.700, IA at 0.732 and 0.812, R^2 at 0.324 and 0.490, RMSE at 0.57 and 0.55, and ANOVA with p-values of 0.099 and 0.387 for Station1 and Station 2 respectively, substantiate the indistinguishability between the model and observed data in terms of their underlying distributions. This high level of concordance underscores the historical model's efficacy in faithfully replicating the characteristics of the observed data, providing a robust indication of its reliability in emulating real-world phenomena. Nevertheless, a subtle deviation arises in the representation of the historical model, particularly in the left tail of the x-axis ranging from 25 to 26. This deviation may be attributed to

inherent limitations within the model, specifically in accurately capturing temperature ranges at the lower end of the spectrum.
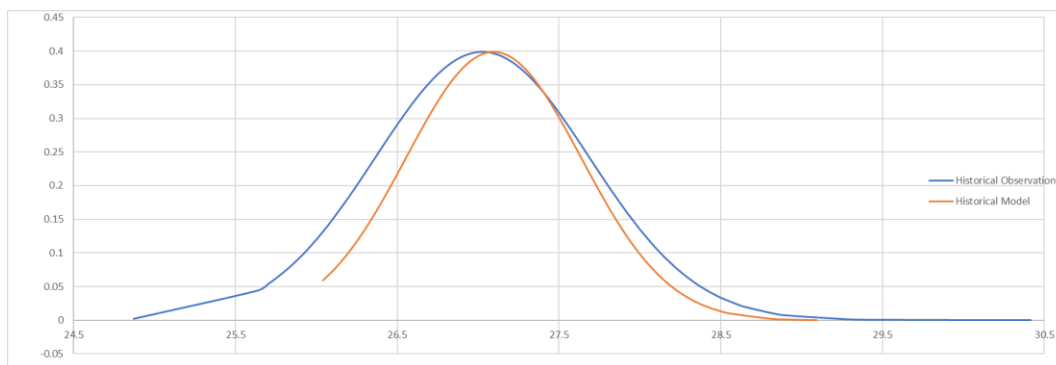
Figure 4.35: Tmax PDF output of Station 1
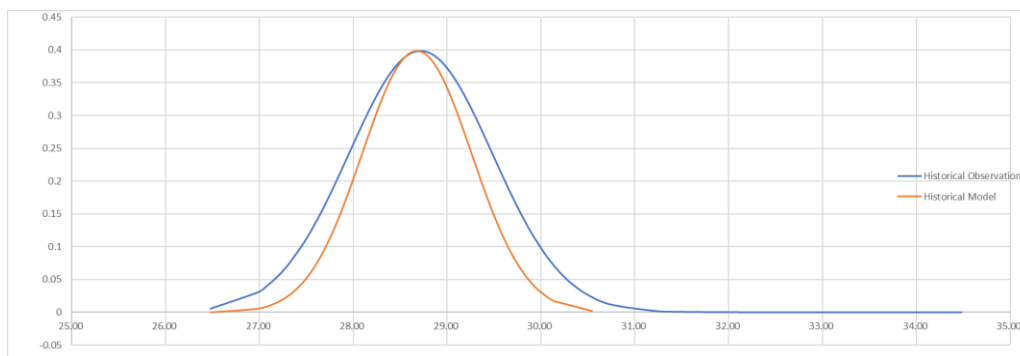
Figure 4.36: Tmax PDF output of Station 2

4.2.3 Temperature at 2 Meters Minimum (Tmin)(C)

Figures 4.37 and 4.38 display the Probability Density Functions (PDFs) illustrating the historical model data juxtaposed with the historical observation data. In Station 1, the Historical Observation Tmin spans from 18.6℃ to 22.62℃, while the Historical Model Tmin data ranges from 18.41℃ to 21.75℃. Conversely, for Station 2, the Historical Observation Tmin encompasses a range from 19.24℃ to 23.95℃, and the Historical Model of Tmin ranges from 19.29℃ to 23.16℃.

In addition to the conspicuous visual alignment observed in the PDFs, quantitative assessments further validate this congruence. Specifically, (PA) values of 0.811 and 0.846, (IA) values of 0.893 and 0.914, (R^2) values of 0.655 and 0.716, (RMSE) values of 0.43 and 0.48, and (ANOVA) results with p-values of 0.811 and 0.782 for Station1 and Station2 respectively, substantiate the indistinguishability between the model and observed data in relation to their underlying distributions.

This notable level of concordance underscores the historical model's proficiency in faithfully reproducing the attributes of the observed data, offering substantial evidence of its reliability in simulating real-world phenomena. However, a subtle discrepancy also emerges in the representation of the historical model like in the Tmax PDFs, particularly in the right tail of the x-axis.
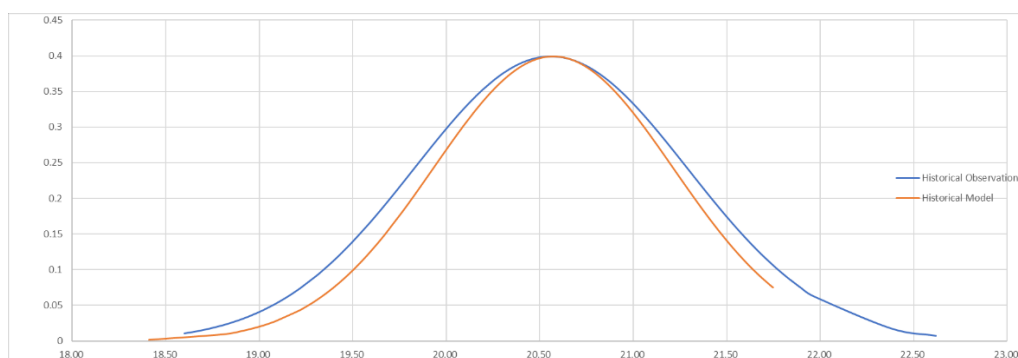
Figure 4.37: Tmin PDF output of Station1
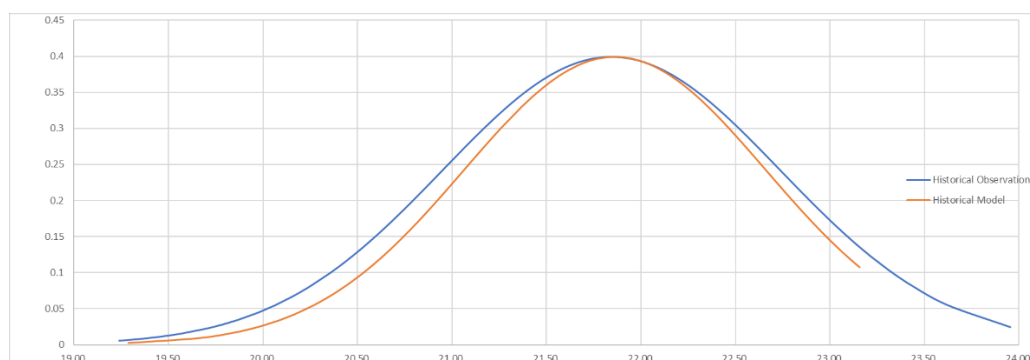
Figure 4.38: Tmin PDF output of Station2

4.2.4Relative Humidity at 2 Meters (%)

Figures 4.39 and 4.40 depict the Probability Density Functions (PDFs) illustrating the historical model data (depicted in orange) in conjunction with the historical observation data (depicted in blue). The x-axis pertains to the humidity variable. In Station 1, the Historical Observation Relative Humidity (RH2M) ranges from 80.12% to 91.9%, while the Historical Model spans from 83.09% to 89.93%. In contrast, for Station 2, the observed RH2M encompasses a range from 88.06% to 93.26%, and the modelled data extends from 88.77% to 90.50%. Quantitative metrics, including (PA) values of 0.585 and 0.470, (IA) values of 0.743 and 0.587, (R^2) values of 0.342 and 0.21, (RMSE) values of 1.52 and 1.76, and (ANOVA) results with p-values of 0.311 and 0.478 for Place 1 and Place 2 respectively, toughly attest to the congruence between the model and observed data in relation to their underlying distributions. Nonetheless, a subtle deviation also arises in the representation of the historical model, akin to what was observed in the Tmax and Tmin Probability Density Functions, particularly in the right tail of the x-axis.
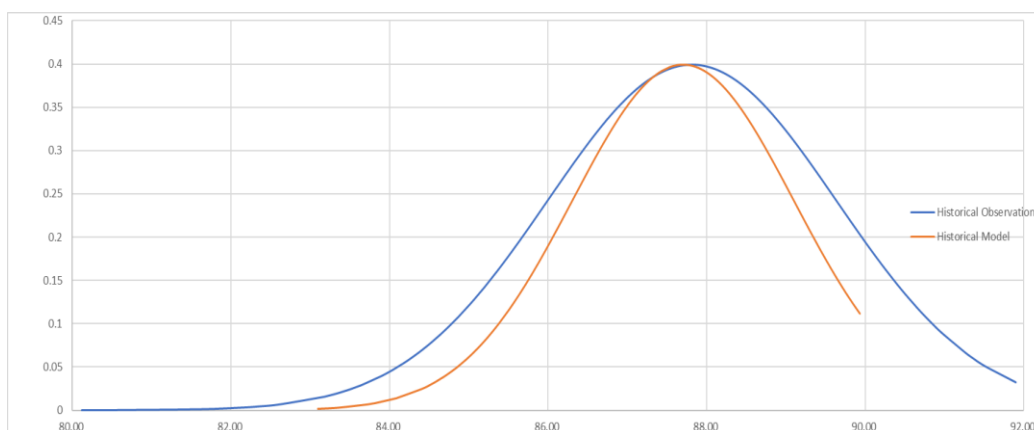
Figure 4.39: Humidity PDF output of Station1
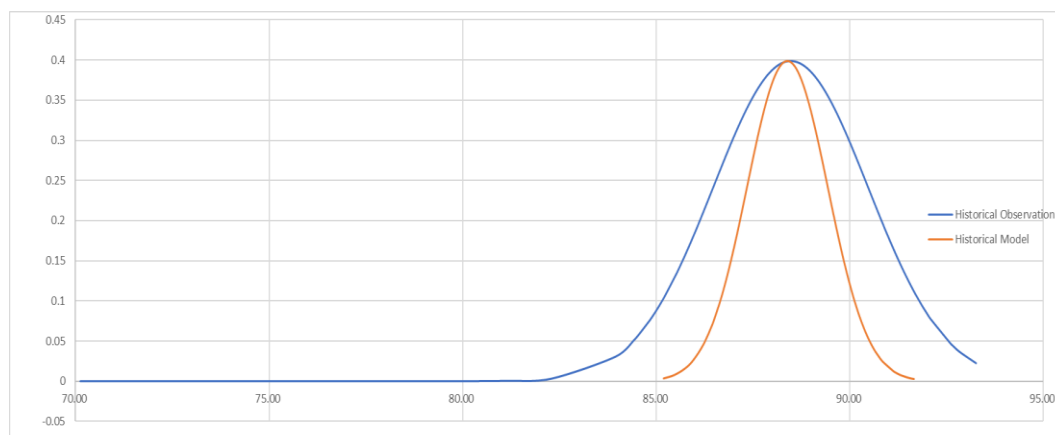
Figure 4.40: Humidity PDF output of Station2

Followed conclusion from above picture，Correlation examinations are employed to assess the linear interdependence between model prognostications and factual observations. for the bias-corrected precipitation and humidity, the correlation between the model and the factual values evinces greater robustness at the Station 1which is 0.4035, 0.342 respectively more than 0.383, 0.21 in Station 2. Conversely, for the Temperature maximum and Temperature minimum, coefficient of determination of Station2 (0.49, 0.716) higher than point 1(0.324, 0.655), potentially signifying heightened precision.

The Root Mean Square Error (RMSE) serves as a metric quantifying the level of disparity between model prognostications and empirical observations. for the bias-corrected precipitation and temperature maximum, the RMSE of model deployed at the secondary place（67.9，0.55）lesser than the Station 1（70.2，0.57）that manifests superior performance in this context. On the contrary, for temperature minimum and humidity, the RMSE of Station 1（0.43，1.52）lesser than the Station 2（0.48, 1.76），it shows that the difference of historical dataset and observed dataset lesser than Station 2.

The outcomes derived from the Analysis of Variance (ANOVA) evinced outcomes obtained at the Station 2 exhibited statistically greater significance for the

bias-precipitation, Tmax and Humidity, thus intimating the potential for heightened accuracy.

4.3 Local climate model generation (2015-2100)

4.3.1 Precipitation

According to Figure 4.41, the grey curve representing observational data for the period from 2015 to 2021 exhibits significant fluctuations, starting at 2255.47 mm in 2015, reaching its first peak of 3080.32 mm in 2017, dropping to its second lowest point of 2280.12 mm in 2019, and subsequently experiencing a rapid ascent to second zenith of 2956.34mm in 2021. Notably, the maximum observed precipitation of 3080.32 mm surpasses the projected annual precipitation values from 2015 to 2100 under the SSP2-4.5 scenario indicated by the blue curve and surpasses the projected annual precipitation values from 2015 to 2080 under the SSP5 indicated by the orange curve, and is 1.05 times greater than the highest projected precipitation of 2930.55 mm in the year 2097 under the SSP2-4.5 scenario.

Based on Figures 4.41 and 4.42, the projected future rainfall under the SSP2-4.5 and SSP5-8.5 scenarios demonstrates a stable increase with slight fluctuations from 2015 to 2100. This stands in contrast to the historical observed rainfall, which exhibited a range of fluctuations from a minimum of 2235.37 mm in 2016 to a maximum of 3080.32 mm in 2017; Over an extremely short one-year period, the precipitation variation amounted to 844.95 mm. However, the anticipated annual precipitation, as projected, does not undergo such extreme changes within a single year.

The Figure 4.41 and 4.42 illustrate the rainfall patterns in the two Stations exhibit remarkable uniformity and stability, devoid of any instances of extreme conditions. One plausible explanation for this observation could be the limited spatial resolution of the data. The absence of records pertaining to extreme conditions, especially in regions characterized by complex topography or intricate rainfall distributions such as the Cameron Highlands, suggests that an enhancement in spatial resolution may facilitate a more precise simulation of local extreme events. It is also conceivable that extreme rainfall occurrences are contingent upon specific weather and climatic phenomena, such as monsoons and cyclones, which were not explicitly

integrated into the model over the fifty-year, or even century-long, period. The manifestation of extreme events may be influenced by non-linear factors such as atmospheric humidity and sea temperature. Considering Malaysia's geographical place in proximity to both the Pacific and Indian Oceans, along with the influence of sea temperature, these non-linear factors warrant inclusion in the model.

Moreover, the model should undergo periodic updates to ensure its sustained accuracy. An additional conjecture posits that the absence of extreme precipitation events from 1983 to 2014 might be attributed to the emergence of extreme climate conditions post-2014, possibly influenced by urbanization, deforestation, inadequate land management, and expansion of crop fields, however from 2015 to 2021 year which is very short as input file for output future model. Therefore, in order to get more accurate projected annual precipitation, it is very crucial that having a long period of time with real extreme precipitation as input learning file. There is a speculation, Perhaps, the proposed approach of combining real observational data from 1983 to 2014 with non-linear factors (2015-2021), such as flash floods, monsoon, El Niño, La Niña, influenced to some extent by urbanization, deforestation, inadequate land management, and expansion of crop fields, to generate simulated historical observation data (1983-2021) for the future climate model is plausible.

However, several considerations must be taken into account. Firstly, the quality of the data is paramount, ensuring that the real observational data from 1983 to 2014 is of high quality and consistency. Simultaneously, it is essential to verify the accuracy of the non-linear factors and their representation in the model. Secondly, the validation of the generated simulated historical observation data against independent observational data is imperative to assess the model's accuracy and reliability. Thirdly, there is a need to assess the consistency of temporal trends and patterns in the combined data to ensure that the model captures realistic changes over time. Fourthly, it is crucial to model the influence of non-linear factors accurately, reflecting their impact on precipitation patterns, and to consider uncertainties in the relationships between non-linear factors and precipitation. It is noteworthy that the assumption of stationarity may not hold, and the relationships between non-linear factors and precipitation may evolve over time. Lastly, consideration should be given to the complexities of urbanization, deforestation, and land management changes, along with their dynamic interactions with climate variables.

Additionally, the model's ability to project future climate conditions relies on the assumptions made during the simulation, and uncertainties may exist.

Refer to Figure 4.41, it is important to highlight that both the blue and orange curves exhibit a positive linear trendline with equations y = 4.3662x – 6334.7 and y = 10.067x - 17902, respectively. The R^2 (coefficient of determination) values increase from 0.7225 to 0.9186. In statistical terms, R^2 signifies the proportion of the total deviation that can be explained by the regression sum of squares, when performing linear regression analysis using the least squares method for parameter estimation. A higher R^2 indicates a more accurate and significant regression effect, with values closer to 1 implying a better fit. Generally, a model with a goodness of fit exceeding 0.8 is considered to be high; hence, this prospective model offers greater accuracy when analysing precipitation patterns under the SSP5-8.5 scenario.
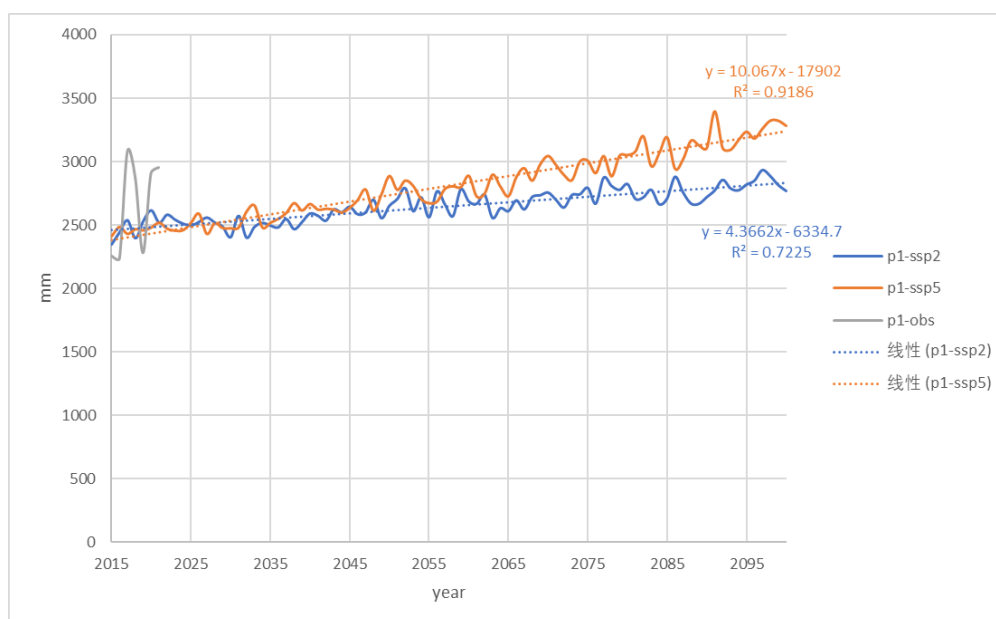
Figure 4.41：Projected Annual Precipitation (2015-2100) based on SSP2-4.5, SSP5-8.5 and observation (2015-2021) of Station 1

Based on Figure 4.42, the noteworthy observation is that both the orange and blue curves exhibit a positive linear trendline represented by the equations y = 4.3923x – 6407 and y = 9.2738x - 16292, respectively. Furthermore, the coefficients of determination (R^2) show an increase from 0.7476 to 0.9181. A higher R^2 indicates a more accurate model

and a more pronounced regression effect. Consequently, this model demonstrates increased accuracy when analysing precipitation patterns under the SSP5-8.5 scenario.

As depicted in Figure 4.42, the curve (p1-obs) representing observational data for the period spanning from 2015 to 2021 displays significant fluctuations, commencing at 2176.41 mm in 2015, reaching its initial peak of 3232.08 mm in 2017, descending to its second lowest point of 2172.03 mm in 2019, and subsequently experiencing a sharp ascent to its second zenith of 3096.66 mm in 2021. It is of particular note that the maximum observed precipitation of 3232.08 mm exceeds the projected annual precipitation values from 2015 to 2100 under the SSP2-4.5 scenario, as indicated by the orange curve. Furthermore, the maximum observed precipitation of 3232.08 mm firstly is surpassed by the projected precipitation in 2091 which is 3328.87 mm under the SSP5-8.5 scenario.
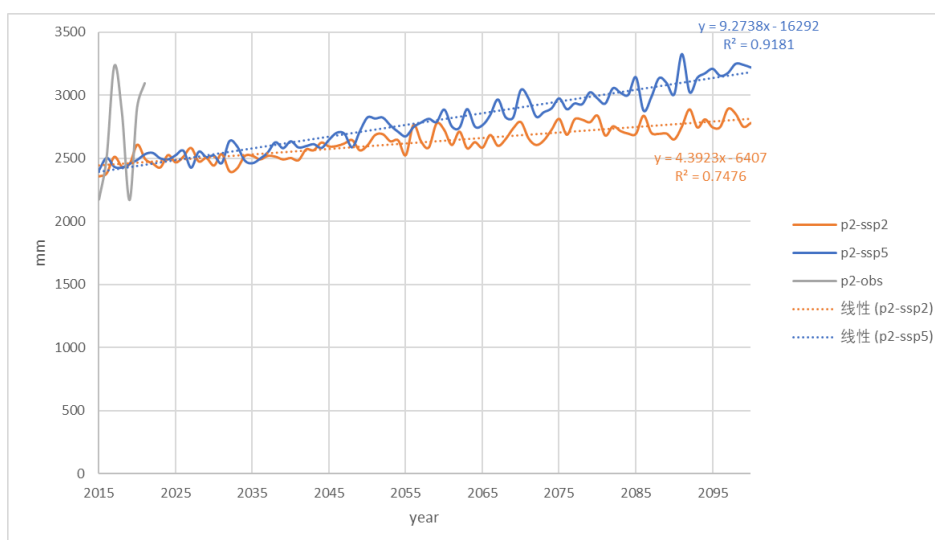
Figure 4.42: Projected Annual Precipitation (2015-2100) based on SSP2-4.5, SSP5-8.5 and observation (2015-2021) of Station 2
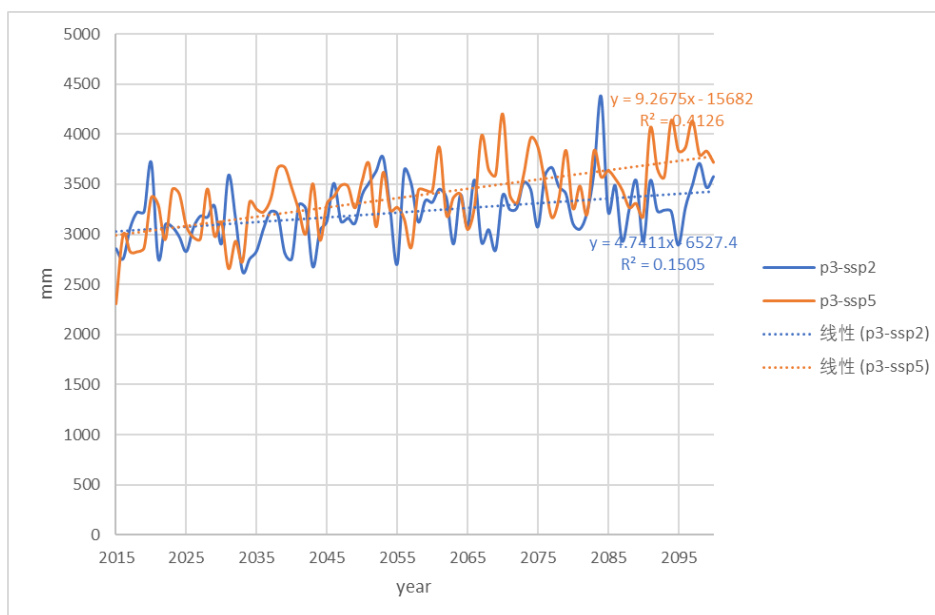
Figure 4.43：Projected Annual Precipitation (2015-2100) based on SSP2-4.5 and SSP5-8.5 of Station 3(MMD)

In Figure 4.43, the curve (p3-ssp2) illustrates variations in rainfall from 2015 to 2100 under the SSP2-4.5 scenario. With an R^2 value of 0.1505, it is noteworthy that the minimum recorded rainfall of 2626.77 mm is approximately 1.7 times lower. The curve (p3-ssp5), representing rainfall changes from 2015 to 2100 under the SSP5-8.5 scenario, demonstrates greater stability with an R^2 value of 0.4126. The maximum recorded rainfall in 1986 was 4199.65mm, which is about 1.8 times the minimum recorded rainfall of 2302.32 mm. By comparing Figures 4.41 and 4.42, it can be deduced that for rainfall variations from 2015 to 2100 under SSP2-4.5 and SSP5-8.5 scenarios, the ratio of maximum to minimum rainfall is approximately 1.25 and 1.4, respectively. Similarly, at Station2, the maximum to minimum rainfall ratio is approximately 1.23 and 1.4, respectively. This indicates that in 1986, the SSP5-8.5 scenario exhibited a greater proportion of maximum to minimum rainfall compared to the SSP2-4.5 scenario.

The MMD data relies predominantly on its dedicated meteorological observation network, encompassing meteorological radar, satellites, meteorological stations, and field data collection by on-site observers. Its primary

objective is to provide precise meteorological information and localized weather forecasts for Malaysia, addressing the meteorological requirements of local residents, businesses, and governmental entities. As depicted in Figure 4.44, it is evident that the projected future rainfall generated by MMD exhibits substantial fluctuations, ranging from 2250 mm to 4500 mm. Notably, the projected annual rainfall from 2015 to 2100 significantly surpasses the historical records. Consequently, it can be reasonably posited that utilizing MMD's historical observation data as a baseline, the resultant local climate model proves to be more accurate and suitable for forecasting future rainfall changes in Malaysia, particularly in the specific context of the Golden Marun Plateau. In contrast, the NASA Power project leverages satellite remote sensing data and meteorological model information on a global scale, emphasizing global energy resources forecasting. Given the broader scope, precision may be comparatively diminished. Hence, MMD stands out as a more fitting choice for developing a localized future climate model for the Cameron Highlands compared to NASA POWER.
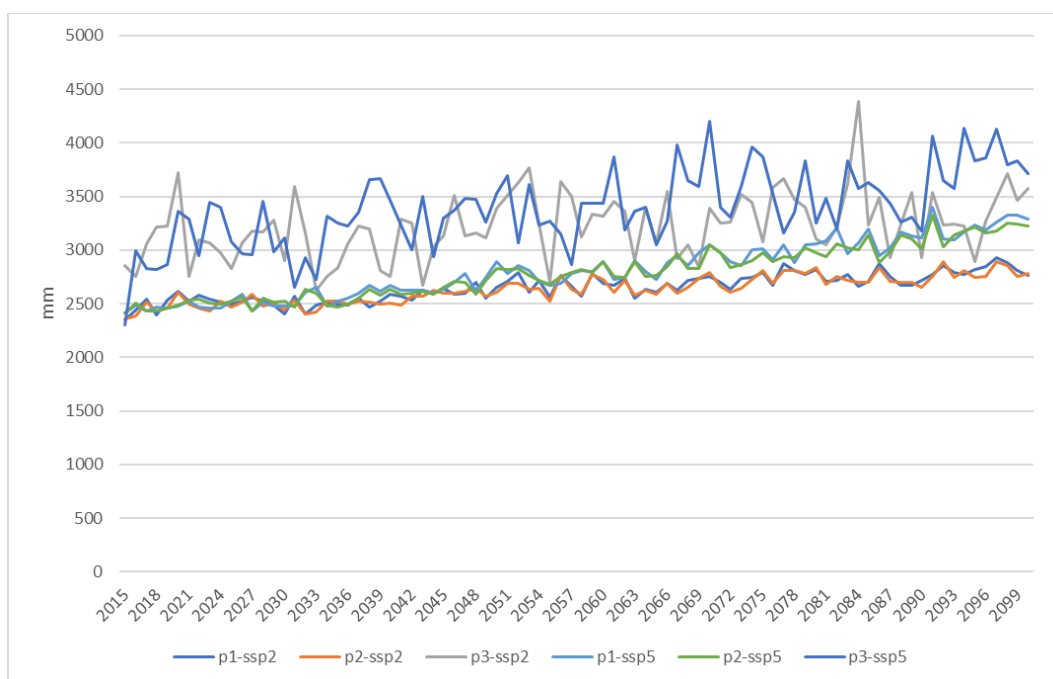
Figure 4.44: Projected Annual Precipitation(2015-2100) based on SSP2-4.5 and SSP5-8.5 of three Station

Anomaly analysis involves subtracting the average historical observed annual rainfall data from 2015 to 2021 for Station 1 and 2 from the predicted rainfall data under the scenarios SSP2-4.5 and SSP5-8.5 from 2022 to 2100. This process aims to highlight anomalies or deviations from the historical average. The results are then presented in four sets of bar charts. Each set of bar charts corresponds to a specific combination of Station and emission scenario (SSP2-4.5 or SSP5-8.5). The x-axis represents the years from 2022 to 2100, and the y-axis represents the anomaly values; Each bar in the chart corresponds to the anomaly for a specific year.

In the context of the identical SSP2-4.5 scenario, a comparative analysis of rainfall anomalies between Station 1 and Station2 reveals distinctive patterns. The maximum negative anomaly at Station 1 is estimated to be approximately -250mm, while at Station 2, it is observed to be in the vicinity of -300mm. In contrast, the maximum positive anomaly at Station 1 is approximately 270mm, whereas at Station2, it is approximately 180mm. Furthermore, an examination of the areas enclosed by the P1-sspP2-4.5 and P2-ssp2 curves in relation to the x-axis reveals noteworthy differences. Specifically, the area corresponding to negative anomalies at Station 2 significantly surpasses that of Station 1, while the area associated with positive anomalies at Station1 is markedly greater than that at Station2. In summary, Station1 is confronted with a heightened risk of extreme rainfall events compared to Station 2.
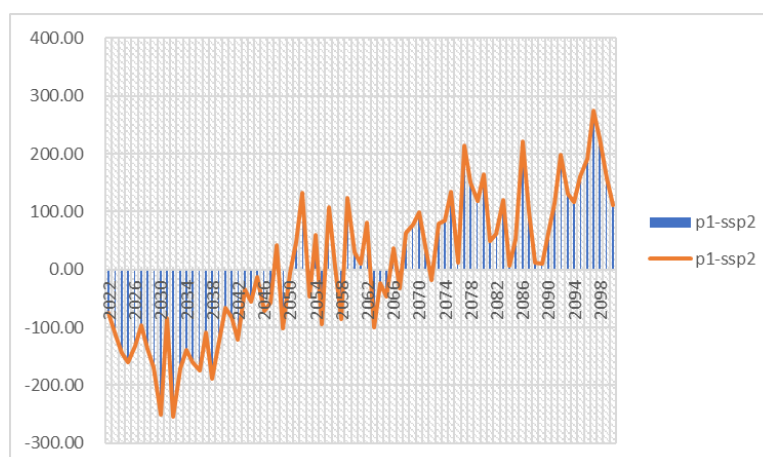
Figure 4.45: Anomaly Variation of precipitation of Station 1 based on

SSP2-4.5 (2022-2100)

According to Figure 4.46, the distribution of anomalous rainfall at Station 2 under the SSP2-4.5 scenario exhibits an inverted iceberg shape, with the majority of negative anomalies concentrating between 2022 and 2055. From 2055 to 2091, the fluctuation of anomalies revolves around the x-axis, while positive anomalies exhibit substantial variation, dropping below the y-axis between 2058 and 2090. The peak value of positive anomalies reaches approximately 180mm. Figure 4.48 illustrates the anomalous rainfall distribution at Station 2 under the SSP5-8.5 scenario, where negative anomalies are primarily concentrated between 2022 and 2049, with the last negative anomaly occurring in 2055. Positive anomalies show a continuous upward trend from 2056 to 2100, with fluctuations but no instances falling below 0mm. The peak value of positive anomalies surpasses 600mm, occurring in 2091. It is evident that under the SSP5-8.5 scenario, simulated rainfall exhibits an earlier onset of positive growth compared to the historical average. Comparing the areas enclosed by the P2-SSP2 and P2-SSP5 curves with the x-axis, the area below the x-axis in the former is significantly greater than in the latter. In the comparison of areas above the x-axis, the latter is significantly greater than the former. These observations suggest that under low-emission scenarios, the likelihood and potential impact of simulated rainfall influenced by extreme precipitation are lower than under high-emission scenarios.

For Figures 4.47 and 4.48, the occurrence of maximum positive anomalies exceeding 600mm indicates an increased flood risk, especially in areas with poor drainage systems or low-lying regions (both Station 1 and Station2 are low-lying areas). Excessive rainfall, while crucial for crop growth in the numerous plantations in the Cameron Highlands, may lead to waterlogging, nutrient leaching, and other agricultural challenges. Intense and prolonged rainfall increases the risk of soil erosion and landslides, particularly in hilly or mountainous areas, where excess water saturates the soil, making it more

susceptible to erosion and slope instability. Heavy rainfall can impact infrastructure such as roads, bridges, and buildings, while increased runoff and flooding may cause damage and disruptions in transportation and other services. Certainly, above-average rainfall has positive implications for water resources, resulting in rising water levels in reservoirs, lakes, and aquifers. This can be advantageous for water supply and agricultural irrigation but may pose challenges in managing excess water resources.
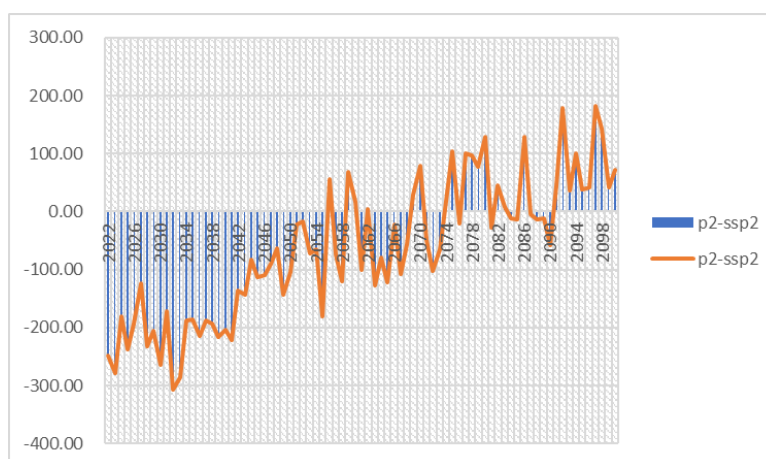
Figure 4.46：**Anomaly variation of precipitation of Station 2 based on SSP2-4.5 (2022-2100)**
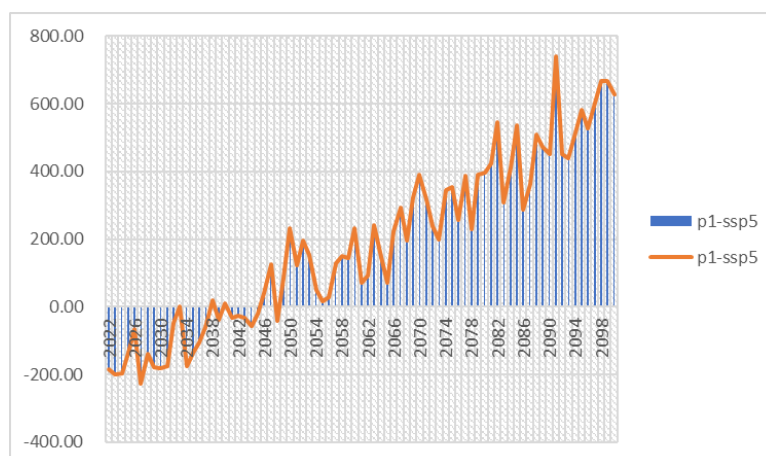
Figure 4.47：Anomaly Variation of precipitation of Station 1 based on

SSP5-8.5 (2022-2100)
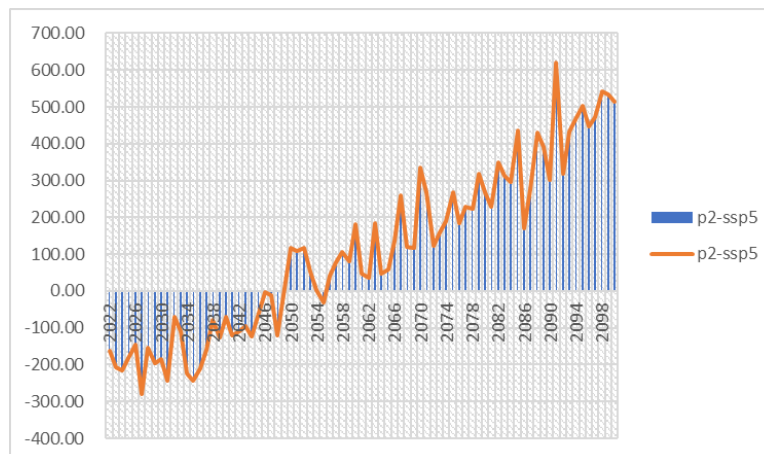
Figure 4.48：Anomaly Variation of precipitation of Station2 based on

SSP5-8.5(2022-2100)

4.3.2 Maximum Temperature (Tmax)

In accordance with Figure 4.49, the L1-Tmax-Obs and L2-TMax-Obs graphs represent the observed historical maximum temperature data for Station 1 and 2 from 2015 to 2022, with average maximum temperatures of 27°C and 29°C, and maximum values of 27.6°C and 29.5°C, respectively. The deep blue and orange lines depict the predicted Temperature maximum data for place 1 under the SSP2-4.5 and SSP5-8.5 scenarios from 2015 to 2100, starting at 27.04°C and 27.05°C, respectively. It is visually apparent that in both scenarios, the predicted data surpass the historical average of 27°C, notably in SSP5-8.5 where the predictions equal the historical maximum in 2096 and 2100. The line (L2-Tmax- SSP2 and L2-Tmax-SSP5) represent the predicted Temperature maximum data for Station 2 under the SSP2-4.5 and SSP5-8.5 scenarios from 2015 to 2100, starting at 28.68°C and 28.76°C, respectively. Predictions under SSP2-4.5 remain below the historical average of 29°C, while under SSP5-8.5, predictions exceed the historical average from 2067 onwards, indicating a potential increase in the frequency of extreme temperature events under this scenario. However, in both

scenarios, the predicted data do not surpass the historical maximum values, emphasizing that model predictions should be regarded as possibilities rather than deterministic future forecasts.

Considering the differing geographical places of Station 1 and 2, with historical average maximum temperatures of 27°C and 29°C, respectively, it suggests that Station 2 may inherently be situated in a hotter climate zone. This difference may be associated with local topography, elevation, and other factors influencing the baseline temperature. Overall, the SSP5-8.5 emission scenario seems more suitable for predicting maximum temperature changes in Station 1 and 2, aligning with the historical extreme temperature events observed in both places.

Upon coarse observation of the four lines' fluctuation patterns, starting around 2060, the predicted temperatures for both places no longer intersect under the two scenarios. This suggests that this point may be a critical threshold. Around 2060, there might be a non-linear transformation in the climate system, leading to a more dispersed prediction of temperatures under both scenarios. This could be indicative of triggered positive feedback mechanisms or threshold effects, accelerating the rate of temperature increase. Regional responses to climate change may also be localized, with 2060 being a pivotal time for regional climate system changes.
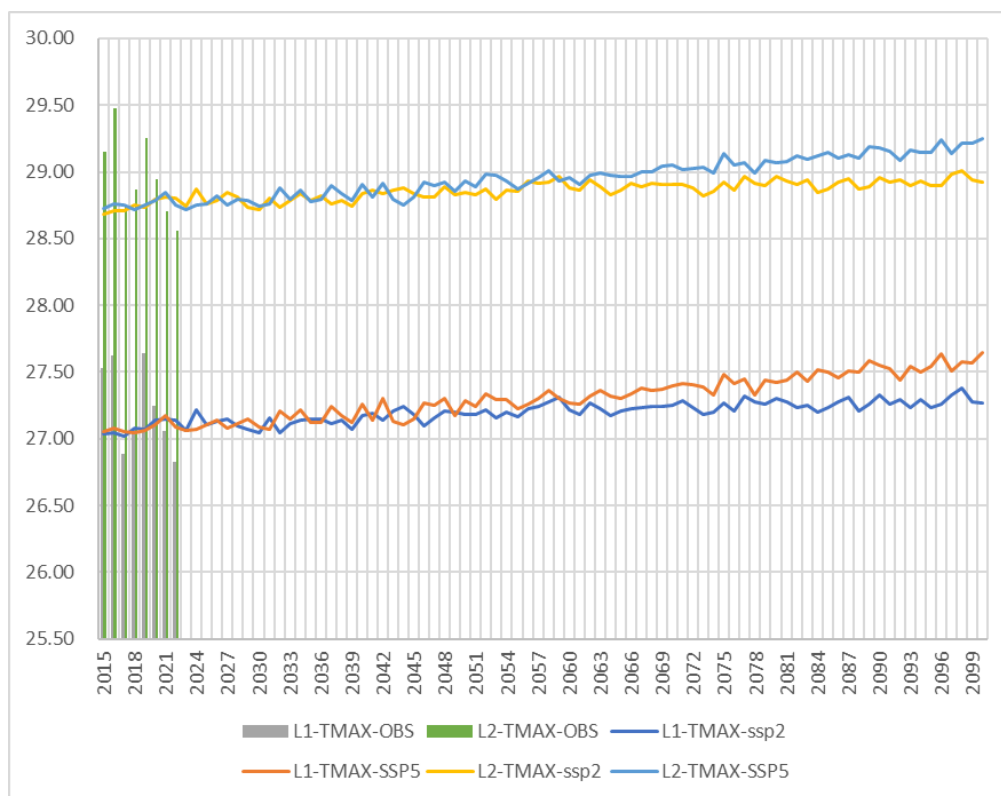
Figure 4.49: Projected Annual Tmax (2015-2100) based on SSP2-4.5, SSP5-8.5 and historical observation (Obs) (2015-2022) for Station 1 and 2

4.3.3 Minimum Temperature (Tmin.)

According to figure 4.50, the observation dataset of Tmin (2015-2022) cannot perfectly match the local climate model generation in SSP2-45 and SSP5-85 scenario (2015-2100). In this study, applying the bias correction, delta method, to correct the 2015-2100 monthly modelled dataset. The argument laid on the historical modelling that could fit perfectly the observation datasets for the Tmax, however, the future climate model is unideal. In fact, it has been stated in many studies that the past climate is not always a good indicator of future performance (Charles et al., 1999; Christensen and Christensen, 2007; Maraun et al., 2010).
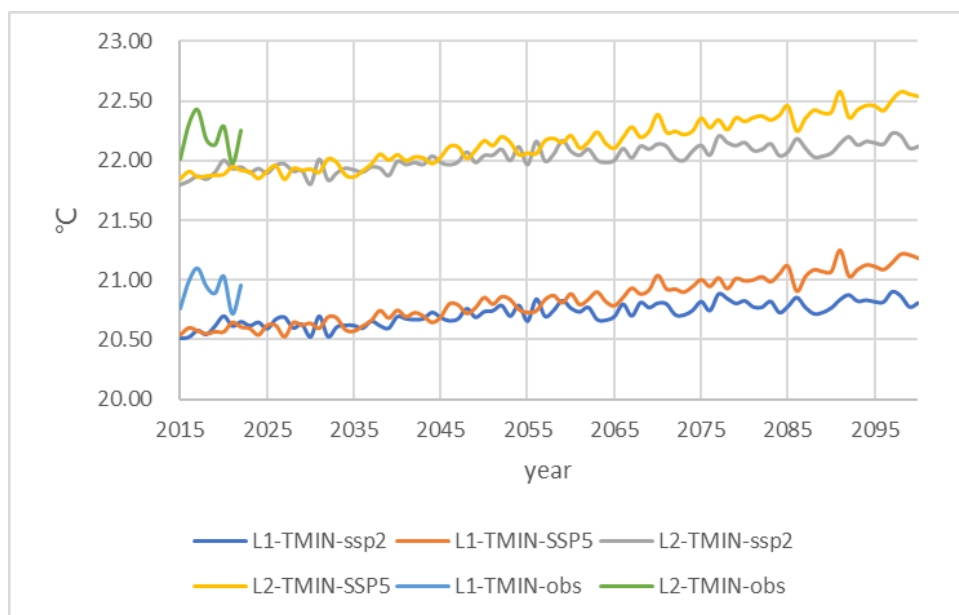
Figure 4.50：Projected Annual Tmin (2015-2100) Based on SSP2-4.5 and SSP5-8.5 of Station 1 and 2

After employing the delta method to adjust the modelled data based on SSP2-4.5 and SSP5-8.5 for two places (as shown in Figure 4.3.3.2), it is evident that the biased correction method has effectively aligned the historical observed data with the historical modelled data. This alignment is due to the historical data consistently fluctuating around the modelled data, significantly enhancing reliability. Notably, two accurate predictions emerged: in the SSP5-8.5 scenario, the predicted minimum temperature for Station 2 in the year 2018 was equal to the observed value, and in the SSP2-4.5 scenario, the predicted minimum temperature for Station 1 in the year 2020 was equal to the observed value.

For Tmin. the fluctuation distances of historical observed values (2015-2022) at Station 1 and 2 are 0.37°C and 0.45°C, respectively. It is worth noting a 4-year difference between the occurrence of the highest peak (2017) and the lowest trough (2021). Regarding Tmax, the fluctuation distances for places 1 and 2 are 0.81°C over a 3-year period and 0.91°C over a 6-year period, with a 4-year difference between the highest (2017) and the lowest peak (2021). A comparative

analysis reveals that historical observed fluctuations are greater, with an average of 0.86°C, exceeding the average fluctuation distance of 0.41°C for historical observed Tmin.. This suggests that Tmax. exhibits more significant fluctuations and a broader range, indicating greater instability compared to Tmin.. However, for both Tmax. and Tmin., the models generated under SSP2-4.5 and SSP5-8.5 scenarios show subdued temperature fluctuations for both places. Moreover, there are no occurrences of fluctuation distances exceeding or equalling the corresponding historical observed values within the 3 to 6-year period. This may be attributed to potential limitations in the model's ability to handle extreme temperature fluctuations. The model's performance can be influenced by factors such as its structure, training data, and the climate model employed. The model may not have effectively captured extreme temperature events present in historical observations (1983-2014). Additionally, calibration using historical observed values (1983-2014) may not have accounted for significant temperature changes post-2014, influenced by factors such as population growth, tourism development, replacement of trees with crops, and elevated atmospheric carbon dioxide levels. These factors may induce non-linear responses in the climate system, especially causing abrupt changes in the short term. If these factors were inadequately considered in the model's training data, the model may struggle to accurately simulate future climate changes.

For Station 1, in the SSP2-4.5 and SSP5-8.5 scenarios, the predicted years for Tmin. to reach or exceed the historical observed highest point are 2048 and 2046, respectively. For Station 2, in the SSP2-4.5 and SSP5-8.5 scenarios, the predicted years are 2056 and 2050, respectively.
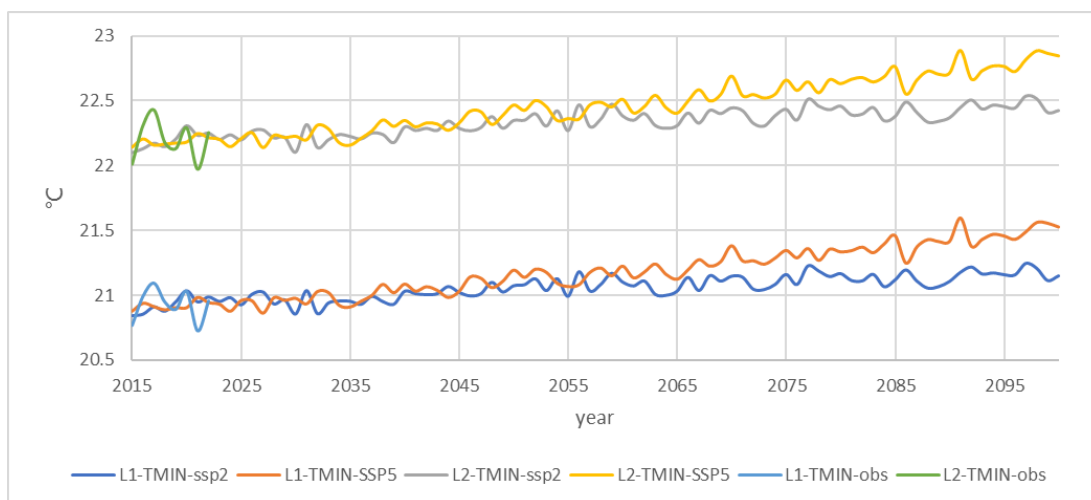
**Figure 4.51：Projected Annual Tmin (2015-2100) Based on SSP2-4.5 and
SSP5-8.5 of Station 1 and2(after biased correction)**

4.3.4 Relative Humidity

For Station 1 and 2, in order to output the projected relative humidity from 2015
to 2100 based on SSP2-4.5 and SSP5-8.5. The historical calibration   file of
humidity which using historical observed data (from 1983 to 2014) as predictand
and 500hpa specific humidity (s500) as predictor variable in unconditional
process and choosing monthly type in the SDSM software and the output file will
be used to proceed scenario generator of future scenario generator of SSP2-4.5
and SSP5-8.5. Based on the figure 4.52, the fluctuation trend of observed data
(2015 - 2022) experienced repetitive fall and rise which assembles a wave and
the later height of wave is higher than prior wave; Furthermore, the change of
historical data enwinds that of the future data; from January to May, November
to December the trend is congruous between projected monthly humidity of nine
groups and observed humidity; Therefore, the future model of humidity is
relatively credible at a qualitive level.

For a more detailed quantitative analysis of relative humidity changes
over years and months, the observed humidity percentages from 2015 to 2019 in
January, May, November, and December intervals were 87.55%, 88.81%,

90.24%, and 89.14%, respectively. These values represent the maximum within their respective intervals, with differences of 0.9%, 0.62%, 1.55%, and 1.04% from the lowest predicted relative humidity in each interval. In February, March, and July to September intervals, the observed humidity percentages from 2015 to 2019 were the lowest compared to other relative humidities within the same intervals, measuring 85.48%, 85.18%, 88.10%, 87.67%, and 87.98%, respectively. The differences from the highest predicted humidity in each interval were 0.98%, 1.67%, 1.12%, 1.67%, and 1.93%. In April, June, and October intervals, the observed humidity percentages from 2015 to 2019 did not significantly deviate from predicted values and remained within the range of predicted humidity percentages.

As the years progress, carbon emissions increase, leading to global warming and climate anomalies, inducing changes in humidity. However, unlike temperature, humidity does not exhibit a straightforward upward trend. Global climate warming may cause an increase in humidity in some regions, while others may experience a decrease. Warmer air has a higher capacity for water vapor, so in certain areas, humidity may increase with rising temperatures. This effect is more pronounced in tropical and subtropical regions, where higher temperatures lead to increased evaporation and water vapor content. Nevertheless, some areas may undergo a decrease in humidity, especially in arid regions, where higher temperatures can accelerate soil moisture evaporation, reducing humidity levels. Additionally, changes in precipitation patterns due to climate change may contribute to decreased humidity in certain areas. The predicted humidity data from 2015 to 2019 for the first group (dark blue line) is at its lowest from March to October, with January, February, November, and December higher than other year groups. The second group (orange line) representing the 2020-2029 period has lower predicted relative humidity in February and November compared to the first group, but higher values for the remaining months. The 2030-2039 period has lower predicted relative humidity in January and December than any of the first two groups, with higher values for the other months. Similarly, the fourth, fifth, sixth, seventh, eighth, and ninth groups show variations in predicted

humidity over different months. The probabilities of negative changes in January and December are highest, as all nine modelled groups exhibit predicted humidity lower than observed group in these two months. February follows with the lowest probability, while March and the months from May to August have positive changes. Therefore, assuming an increase in humidity as positive and a decrease as negative, January and December are more likely to experience negative changes, reflecting the consistency of data variation across different scenarios.

In summary, the findings suggest that humidity changes are influenced by climate warming, and future predictions should consider the complex interplay of factors leading to varied humidity trends in different regions.

	January	Feb	March	April	May	June	July	Aug	Sept	Oct	Nov	Dec
2015-2019	87.06	85.79	85.67	86.81	88.22	88.26	88.69	88.52	88.42	88.63	88.80	88.34
2020-2029	87.07	85.66	86.31	86.92	88.27	88.66	88.87	88.73	88.53	88.97	88.69	88.62
2030-2039	86.92	85.74	86.09	87.28	88.38	88.53	88.86	88.85	88.67	89.08	88.84	88.38
2040-2049	86.90	85.85	86.22	87.46	88.26	88.64	88.98	88.88	88.90	89.24	88.90	88.40
2050-2059	87.02	86.14	86.35	87.54	88.19	88.96	89.19	88.67	88.96	89.43	89.10	88.46
2060-2069	86.81	85.99	86.62	87.59	88.33	89.01	89.12	89.04	88.91	89.39	89.23	88.21
2070-2079	86.76	86.46	86.85	87.64	88.20	88.74	89.02	88.99	89.32	89.40	89.21	88.10
2080-2089	86.65	86.33	86.78	87.77	88.47	89.21	89.18	89.18	89.28	89.46	89.41	88.26
2090-2100	86.76	86.39	86.73	87.89	88.52	88.84	89.22	89.34	89.91	89.65	89.50	88.34
2015-2022 obs	87.55	85.48	85.18	87.19	88.81	88.58	88.10	87.67	87.98	88.74	90.24	89.14

Figure 4.52: Monthly Average Relative Humidity Based on SSP2-4.5 of Station1

Comparing Figures 4.52 and 4.53, it is visually evident that the 10- years monthly average predicted humidity   from 2015 to 2100 under the SSP5-8.5 scenario exhibit more dispersion than those based on the SSP2-4.5 scenario. This implies that under the SSP5-8.5 scenario, there is a larger difference in humidity percentages among different annual periods, likely due to the anticipated high population growth, intense economic development, and extensive energy use, leading to higher levels of greenhouse gas emissions. In this scenario, the impacts of climate change may be more severe, resulting in more significant variations in humidity. In contrast, the assumptions under the SSP2-4.5 scenario involve milder socioeconomic development and lower greenhouse gas emissions, suggesting relatively minor climate impacts and more stable humidity changes among different annual periods. In general, scenarios play a crucial role in predicting future climate changes. Different scenarios lead to varying degrees of humidity changes, resulting in distinct dispersion trends.

Assuming an increase in humidity with each subsequent year as positive change and a decrease relative to the previous year as negative change, the 2015-2019 period exhibits negative changes in predicted humidity for January, May, July, November, and December. The 2020-2029 period shows negative changes in predicted humidity for January, July, October, and December. The 2030-2039 period shows negative changes in predicted humidity for January, November, and December. The 2040-2049 period also exhibits negative changes in predicted humidity for January, February, and December. The 2050-2059 period exhibits negative changes in predicted humidity for December. The 2060-2069 period shows negative changes in predicted humidity for February and December. The 2070-2079 period shows negative changes in predicted humidity for January. The 2080-2089 period shows negative changes in predicted humidity for May and October. The 2090-2100 period shows negative changes in predicted humidity for January, March, and November. January and December intervals exhibit the highest frequency of negative changes, and this pattern is consistent in both SSP5-8.5 and SSP2-4.5 scenarios, reflecting a similarity in data variation between the two scenarios.

Quantitative analysis based on the SSP5-8.5 scenario reveals a relationship between predicted and observed and relative humidity. In January, the observed relative humidity (2015-2022) is recorded as the highest values within that interval, while in February, March, July, August, September, and October, the observed humidity from 2015 to 2019 is the lowest compared to other relative humidities within the same intervals. This indicates that, compared to the SSP2-4.5 scenario, the monthly average predicted relative humidity from 2015 to 2100 under the SSP5-8.5 scenario is generally higher value.

	January	Feb	March	April	May	June	July	Aug	Sept	Oct	Nov	Dec
2015-2019	87.19	85.70	85.75	86.68	88.50	88.47	88.79	88.45	88.66	89.05	88.70	88.42
2020-2029	86.86	85.85	85.97	87.18	88.37	88.52	88.58	88.67	88.65	89.03	88.98	88.12
2030-2039	86.86	86.10	86.28	87.11	88.47	88.47	88.86	88.73	88.68	89.15	88.89	88.60
2040-2049	87.03	86.06	86.40	87.35	88.39	88.74	88.93	88.97	89.08	89.24	89.31	88.69
2050-2059	87.24	86.41	86.57	87.66	88.54	88.90	89.26	89.34	89.31	89.36	89.58	88.48
2060-2069	87.30	86.28	86.92	87.88	88.61	89.03	89.36	89.60	89.58	89.56	89.72	88.61
2070-2079	87.21	86.91	87.40	87.98	88.82	89.33	89.37	89.77	89.73	89.90	89.80	88.91
2080-2089	87.53	86.93	87.77	88.34	88.77	89.68	89.81	89.82	89.99	89.89	90.32	89.08
2090-2100	87.45	87.27	87.66	88.95	89.04	89.70	90.19	89.96	90.06	90.34	90.31	89.17
2015-2022 obs	87.55	85.48	85.18	87.19	88.81	88.58	88.10	87.67	87.98	88.74	90.24	89.14

Figure 4.53: Monthly Average Relative Humidity based on SSP5-8.5 of Station 1

Through a preliminary comparison of Figures 4.52 to 4.55, it is evident that, in contrast to Station 1, the monthly average predicted data for the nine periods from 2015 to 2100 at Place 2 under the SSP2-4.5 and SSP5-8.5 scenarios exhibit a better fit with the historical observed data from 2015 to 2022. This scenario suggests that the historical humidity data at Station 2 from 1983 to 2014, used as a calibration reference, can yield more accurate future models. Conversely, it indicates that the historical observed data at Station 1 may have lower accuracy

or systemic errors. In both scenarios, for the nine annual groups in January and December, the monthly average predicted values at both Station 1 and   2 underestimate the historical observed relative humidity values from 2015 to 2022. Additionally, for the months of February, March, July, August, September, and October from 2015 to 2022, the historical observed relative humidity values are lower than the corresponding monthly average predicted values. These observations suggest a fundamental similarity in the future predictive models for both Stations.

	January	Feb	March	April	May	June	July	Aug	Sept	Oct	Nov	Dec
2015-2019	89.52	88.35	87.74	86.80	88.27	88.43	88.86	88.54	87.68	87.75	89.50	90.14
2020-2029	89.65	88.32	88.06	87.05	88.39	88.78	88.96	88.77	87.78	88.11	89.53	90.45
2030-2039	89.45	88.23	87.77	87.16	88.42	88.68	89.03	88.84	87.94	88.36	89.72	90.28
2040-2049	89.43	88.38	87.70	87.42	88.27	88.76	89.12	88.69	88.08	88.66	89.83	90.42
2050-2059	89.52	88.42	87.66	87.55	88.21	89.17	89.38	88.48	88.09	88.93	90.19	90.45
2060-2069	89.35	88.29	87.82	87.53	88.36	89.08	89.22	88.80	88.08	89.08	90.33	90.35
2070-2079	89.26	88.52	87.62	87.76	88.28	89.00	89.15	88.59	88.49	89.11	90.36	90.24
2080-2089	89.20	88.44	87.63	87.77	88.50	89.42	89.21	88.81	88.49	89.34	90.64	90.45
2090-2100	89.22	88.46	87.36	87.89	88.59	89.05	89.32	88.82	89.00	89.61	90.84	90.52
2015-2022 obs	90.17	88.47	87.28	87.40	88.48	88.65	88.27	87.89	87.43	87.81	90.72	91.30

Figure 4.54: Monthly average Relative Humidity based on SSP2-4.5 of Station2

	January	Feb	March	April	May	June	July	Aug	Sept	Oct	Nov	Dec
2015-2019	89.74	88.26	87.76	86.76	88.41	88.59	88.88	88.51	87.89	88.12	89.40	90.18
2020-2029	89.43	88.43	87.80	87.15	88.50	88.54	88.72	88.55	87.82	88.10	89.66	90.03
2030-2039	89.42	88.53	87.81	87.08	88.55	88.64	89.07	88.58	87.83	88.42	89.69	90.55
2040-2049	89.54	88.39	87.76	87.48	88.47	88.86	89.04	88.78	88.30	88.57	90.12	90.67
2050-2059	89.74	88.63	87.87	87.70	88.60	89.12	89.49	89.09	88.49	88.91	90.51	90.51
2060-2069	89.70	88.54	87.94	87.96	88.73	89.30	89.56	89.21	88.77	89.09	90.68	90.67
2070-2079	89.65	88.84	88.29	88.13	88.92	89.54	89.53	89.45	88.82	89.51	90.82	91.04
2080-2089	89.91	88.94	88.47	88.41	88.99	90.18	90.20	89.43	89.08	89.67	91.48	91.23
2090-2100	89.81	88.97	88.18	89.10	89.34	90.16	90.46	89.55	89.11	90.08	91.55	91.40
2015-2022 obs	90.17	88.47	87.28	87.40	88.48	88.65	88.27	87.89	87.43	87.81	90.72	91.30

Figure 4.55: Monthly average Relative Humidity based on SSP5-8.5 of Station 2

In Figure 4.56, the   curves （H1-Obs and H2-Obs）represent the historical humidity variations at Station1 and 2 from 2015 to 2022, respectively. It exhibits fluctuations around the corresponding future model (2015-2100) generated for each station. Starting from 2017 until the end of the historical observed data in 2022, it is roughly observed that the gap between the observed humidity data at both places remains nearly constant. Translation in either upward or downward directions results in overlapping states, a condition replicated in the predicted data for both stations under the SSP2-4.5 and SSP5-8.5 scenarios. Based on these phenomena, it can be qualitatively concluded that the predictive models for both places are reliable.

Upon examining the historical observed data, two significant peaks and two significant troughs are evident, with peaks occurring in 2017 and 2020, spaced two years apart, and troughs primarily appearing in 2016 and 2019, also

spaced two years apart. For the predicted data under the SSP2-4.5 scenario at Station 1 and 2, significant peaks mainly occur in 2020, 2048, 2052, 2056, 2060, 2068, 2092, 2095, and 2098. Interestingly, the peak humidity values from 2048 to 2060 occur every four years, while from 2092 to 2098, they occur every three years. Additionally, it is noteworthy that humidity is generally higher from 2076 to 2087. Consequently, it is inferred that with the increase in years, the frequency of extreme humidity occurrences also increases.

For the predicted relative humidity under the SSP5-8.5 scenario at Station 1 and 2, significant peaks mainly occur in 2032, 2037, 2047, 2052, 2056, 2067, 2071, 2076, 2081, 2084, 2089, 2091, 2095, and 2099. A clear distinction between the two scenarios is evident, with the SSP5-8.5 scenario showing a higher frequency and more occurrences of peak humidity values, and the peaks are more irregular and challenging to be predicted in the study.
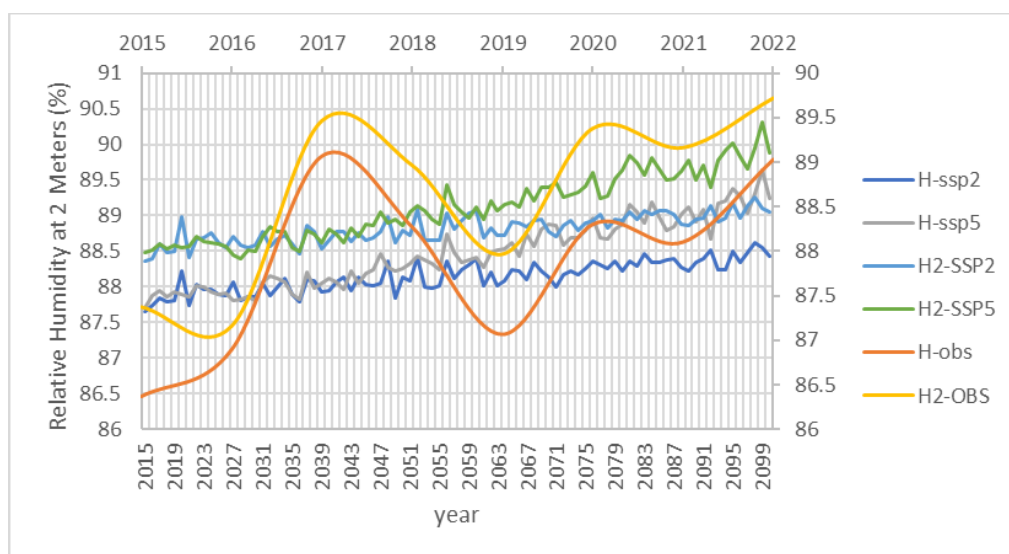
Figure 4.56: Projected and Observed Average Relative Humidity (2015-2100) based on SSP2-4.5 and SSP5-8.5 of Station 1 and 2

4.3.5 Spatial Analysis of Future Precipitation

The Figures 4.57 to 4.64 illustrate the predicted total rainfall distribution at three study sites in Cameron Highlands, Malaysia, based on the SSP2-4.5 and SSP5-8.5 scenarios for the periods 2015-2035, 2036-2055, 2056-2075, and 2076-2100. The Stations labelled as P1, P2, and P3 on the map correspond to the three study station in Chapter 3 , represented by Figure 3.4.2.1 and Figure 3.4.2.2. The former two stations were sourced from NASA Power, while the latter was from the Malaysia Meteorological Department (MMD). Based on the rainfall patterns, it is observed that the higher rainfall at the P3 compared to P1 and P2 which may be attributed to the mountainous terrain, where the higher altitude results in rapid air cooling, conducive to convection, condensation, and precipitation formation. This phenomenon, commonly known as "orographic precipitation," often leads to persistent cloud cover and increased precipitation in certain mountainous regions. Conversely, lowland areas are generally situated at relatively lower elevations and may be shielded by mountain ranges, reducing the chances of moist air ascending, cooling, condensing, and subsequently experiencing less precipitation. However, these are general trends and may not be universally applicable to all highland and lowland areas. Factors such as geographic place, climate region, and topography can significantly influence rainfall patterns. Therefore, rainfall distribution may vary considerably in specific circumstances. Additionally, the arrow in the upper right corner indicates the north direction, while the legend in the lower-left corner, composed of a title and groups represented by different colours, provides information about different rainfall ranges.

Longitudinal comparisons were made for the rainfall variations at places P1, P2, and P3 over year year-span groups (2015-2035, 2036-2055, 2056-2075, 2076-2100) under the scenarios of SSP2-4.5 and SSP5-8.5. The analysis of Figure 4.65's data in conjunction with Figure 4.57 to 4.58 reveals the rainfall distribution at P1, P2, and P3 from 2015 to 2035 under the SSP2-4.5 and SSP5-8.5 scenarios. In the SSP2-4.5 scenario, the rainfall at P1, P2, and P3 is

respectively 2499.73 mm, 2479.74 mm to 3052.79 mm. Under the SSP5-8.5 scenario, the rainfall at P1, P2, and P3 is 2495.32 mm, 2503.08 mm, and 3031.36 mm, with only P2 experiencing a slight increase of 23.34 mm; P1 and P3 witness decreases of 4.41 mm and 21.43 mm, respectively. Examining the data from Figure 4.65 and dynamic changes in Figures 4.59 to 4.60, for the time span group of 2036 to 2055, under SSP2-4.5, the rainfall at P1, P2, and P3 is 2602.83 mm, 2579.54 mm to 3179.17 mm. Under SSP5-8.5, the rainfall at P1, P2, and P3 is 2687.97 mm, 2663.35 mm, and 3367.17 mm. In this group, the rainfall at P1, P2, and P3 is higher under SSP5-8.5 compared to SSP2-4.5, with increases of 85.14 mm, 83.81 mm, and 188.00 mm, respectively. The rainfall increase at P3 is 2.2 times the average increase at P1 and P2. Further considering the data from Figure 4.65 and dynamic changes in Figures 4.61 to 4.62, for the time span group of 2056 to 2075, under SSP2-4.5, the rainfall at the three places is 2689.64 mm, 2675.87 mm, and 3268.68 mm. Under SSP5-8.5, the rainfall increases to 2865.91 mm, 2850.71 mm, and 3499.7 mm, with increases of 176.27 mm, 174.84 mm, and 231.02 mm, respectively. The rainfall increase at P3 is 1.3 times the average increase at P1 and P2. Considering the data from Figure 4.65 and dynamic changes in Figures 4.63 to 4.64 for the time span group of 2076 to 2100, under SSP2-4.5, the rainfall at the three places is 2777.93 mm, 2760.75 mm, and 3379.92 mm.

Under SSP5-8.5, the rainfall increases to 3128.62 mm, 3079.16 mm, and 3606.45 mm, with increases of 350.69 mm, 318.41 mm, and 226.53 mm, respectively. The rainfall increase at P3 is 0.7 times the average increase at P1 and P2. In summary, regarding the temporal trends, over the last three year-span groups (2036-2055, 2056-2075, 2076-2100), the rainfall at P1, P2, and P3 exhibits an increasing trend over time for both SSP2-4.5 and SSP5-8.5 scenarios, while the first year-span group (2015-2035) experiences a decrease in rainfall. One possible explanation is that P1 and P3 under the SSP2-4.5 scenario may be influenced by specific meteorological or environmental factors, resulting in reduced rainfall during this specific period. This may include, but is not limited to, prolonged drought, climate anomalies, or other natural variations. In such

cases, even if the overall trend is an increase, specific places may experience short-term decreases in rainfall during specific time periods. Through scenario comparisons, particularly between SSP2-4.5 and SSP5-8.5, it is observed that in each time span group, the rainfall under SSP5-8.5 is generally higher than under SSP2-4.5. This suggests that higher emission scenarios may lead to greater precipitation when considering climate change. Through place comparisons, in each time span group, the rainfall at P3 is consistently higher than at P1 and P2, indicating that certain regions may be more susceptible to the effects of climate change or are likely to experience greater precipitation in the future. Therefore, when planning future regional development, such as constructing residential or agricultural areas, it is advisable to avoid placing areas susceptible to rainfall impacts in the P3 place. Through incremental comparisons, it is evident that, over time, the incremental increase under SSP5-8.5 gradually surpasses that under SSP2-4.5. Particularly in the later time span groups (2056-2075 and 2076-2100), the incremental increase is relatively large, indicating that climate change under high emission scenarios may lead to more significant rainfall increases.

Longitudinal comparisons were conducted between two scenarios, SSP2-4.5 and SSP5-8.5, regarding the rainfall variations at places P1, P2, and P3 over four 20-years-span groups (2015-2035, 2036-2055, 2056-2075, 2076-2100 period). In the SSP2-4.5 scenario, the rainfall at P1 varied as 2499.73 mm, 2602.83 mm, 2689.64 mm, and 2777.93 mm, with respective increments of 103.1 mm, 86.81 mm, and 88.29 mm. At P2, the rainfall varied as 2479.74 mm, 2579.54 mm, 2675.87 mm, and 2760.75 mm, with respective increments of 99.8 mm, 96.33 mm, and 84.88 mm. For P3, the rainfall varied as 3052.79 mm, 3179.17 mm, 3268.68 mm, and 3379.92 mm, with respective increments of 126.38 mm, 89.52 mm, and 111.24 mm. In the SSP5-8.5 scenario, the rainfall at P1 varied as 2495.32 mm, 2687.97 mm, 2865.91 mm, and 3128.62 mm, with respective increments of 192.65 mm, 177.94 mm, and 262.71 mm. At P2, the rainfall varied as 2503.08 mm, 2663.35 mm, 2850.71 mm, and 3079.16 mm, with respective increments of 160.27 mm, 187.36 mm, and 228.45 mm. For P3, the rainfall varied

as 3031.36 mm, 3367.17 mm, 3499.7 mm, and 3606.45 mm, with respective increments of 335.81 mm, 132.53 mm, and 106.75 mm.

It is noteworthy that in the SSP5-8.5 scenario, the most significant increase in rainfall at P3 is 335.81 mm for Increment 1, which is 1.9 times the average of Increment 1 at the other two places, while in the SSP2-4.5 scenario, it is only 1.3 times. Subsequently, the increase in P3 rainfall significantly decreases to 132.53 mm, then gradually decreases to 106.75 mm. This suggests that, under the SSP5-8.5 scenario, the rainfall variation at P3 is concentrated in the early time span group, followed by a decline. It is evident that under the SSP2-4.5 scenario, the rainfall increment remains relatively stable, with minimal variations at P1, P2, and P3, averaging only 22.69 mm. This may indicate that under lower emission scenarios, the impact of extreme climatic events is less pronounced. However, under the SSP5-8.5 scenario, the rainfall increment variations at P1, P2, and P3 are substantial, with an average of 127.30 mm. This underscores that under high emission scenarios, different places may experience extreme precipitation variations, and such changes may not be uniformly distributed. In summary, the rainfall variations under the SSP5-8.5 scenario are significantly greater than those under the SSP2-4.5 scenario, especially at the P3 . Given the notable changes in rainfall at P3, the government may need to consider implementing urgent climate adaptation and water resource management measures. This could involve strengthening flood prevention measures, improving water resource utilization efficiency, and promoting climate-adaptive planning. Government collaboration with scientists, communities, and stakeholders is essential to formulate comprehensive climate change response strategies. In response to the abrupt changes at P3, a more in-depth risk assessment should be conducted to understand potential impacts, such as flood risks and ecosystem changes. Based on these assessments, more effective and targeted planning and policies can be formulated.
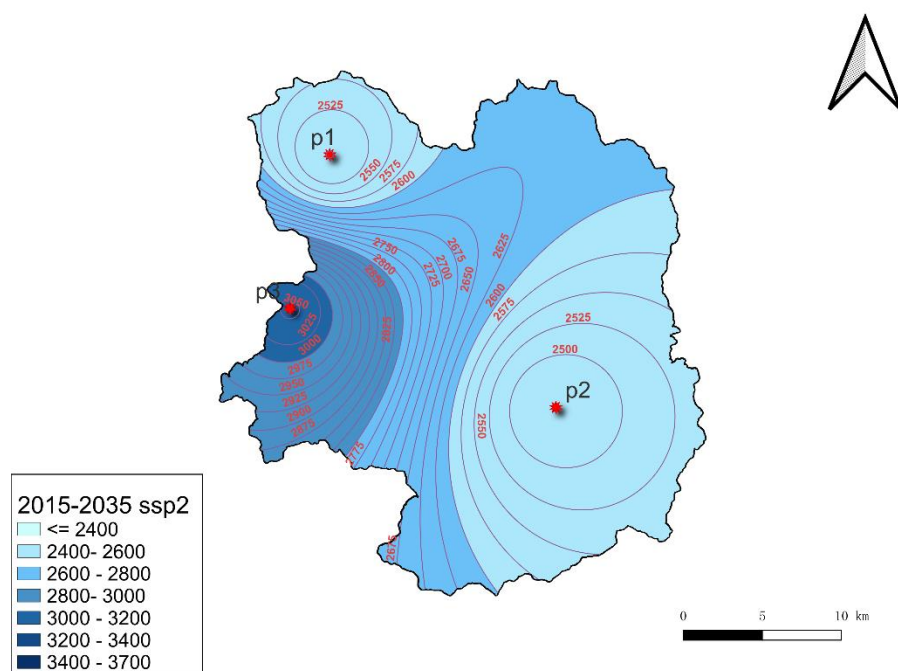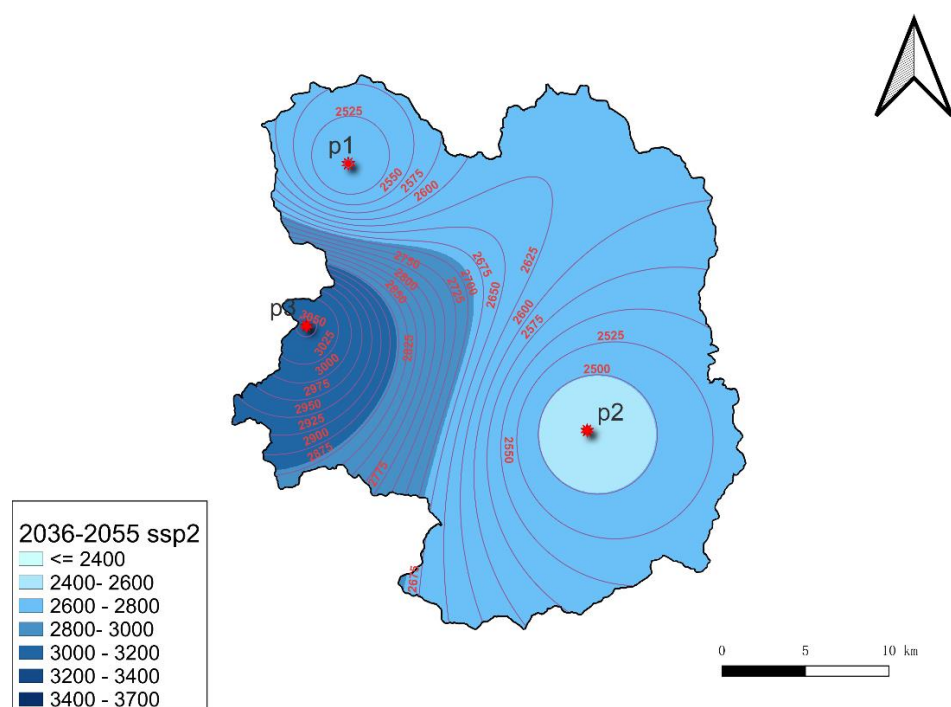
Figure 4.57: Average of Annual Rainfall Pattern of three Stations based on SSP2-4.5 (2015-2035)
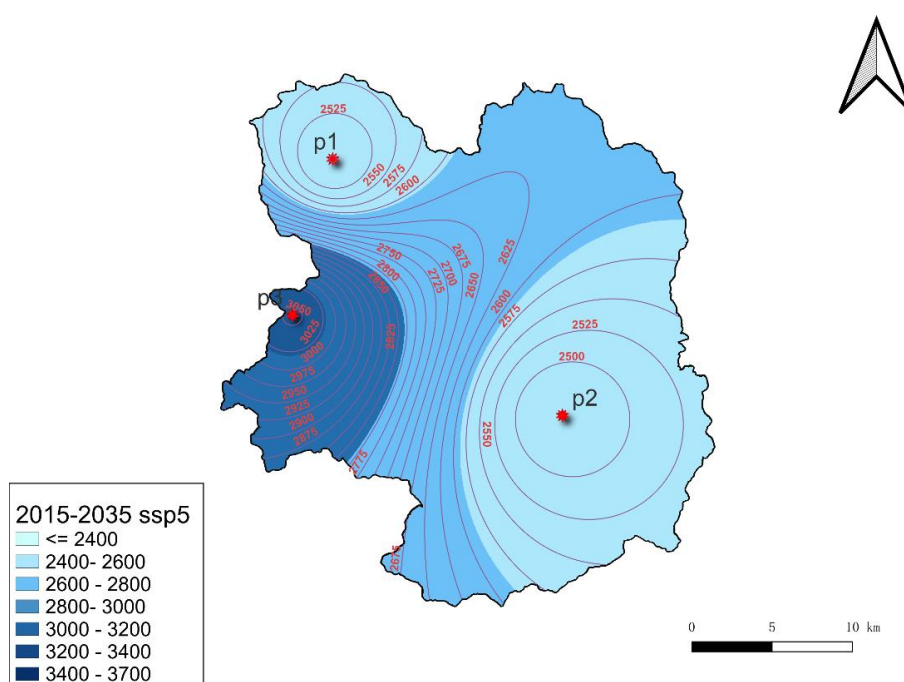
Figure 4.58: Average of Annual Rainfall Pattern of three Stations Based on SSP5-8.5(2015-2035)

According to Figure 4.65, a comparison of precipitation changes between the years 2015-2035 under the scenarios SSP2 and SSP5 reveals a decrease in precipitation at locations P1 and P3, while P2 experiences an increase. Figures 4.57 and 4.58 indicate that the precipitation range of 2400-2600mm is shifting inward towards point P2 and expanding outward at P3. Simultaneously, the precipitation range of 3000-3200mm shows a significant reduction in coverage.

Figure 4.59: Average of Annual Rainfall Pattern of three Stations Based on SSP2-4.5 (2036-2055)
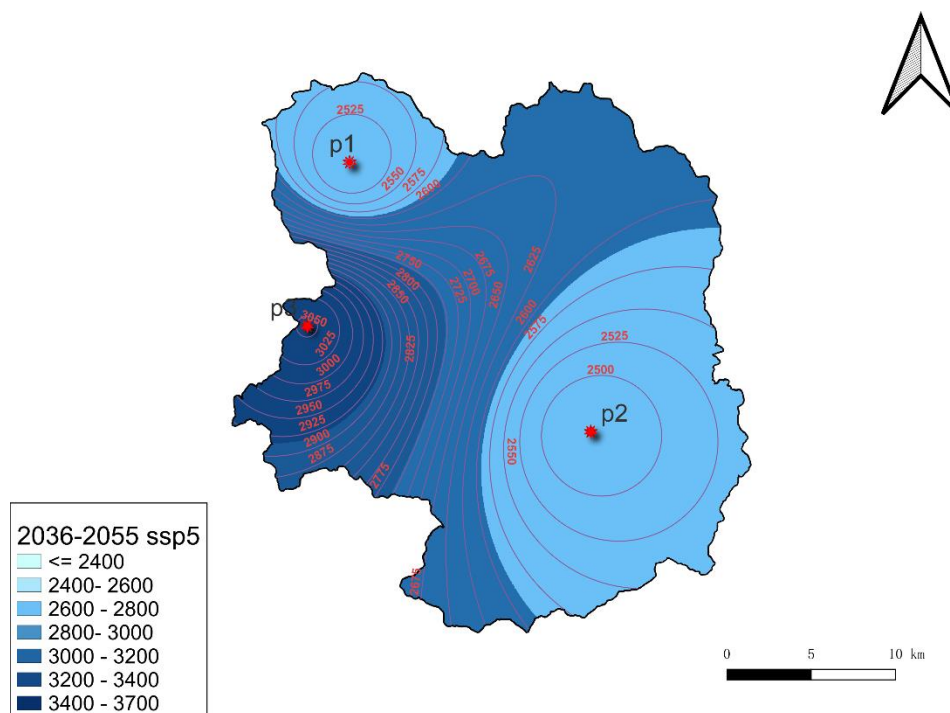
Figure 4.60: Average of Annual Rainfall Pattern of three Stations based on SSP5-8.5 (2036-2055)

Figure 4.61:   Average of Annual Rainfall Pattern of three Stations based on SSP2-4.5 (2056-2075)

Figure 4.62:   Average of Annual Rainfall Pattern of Three Stations based on SSP5-8.5 (2056-2075)
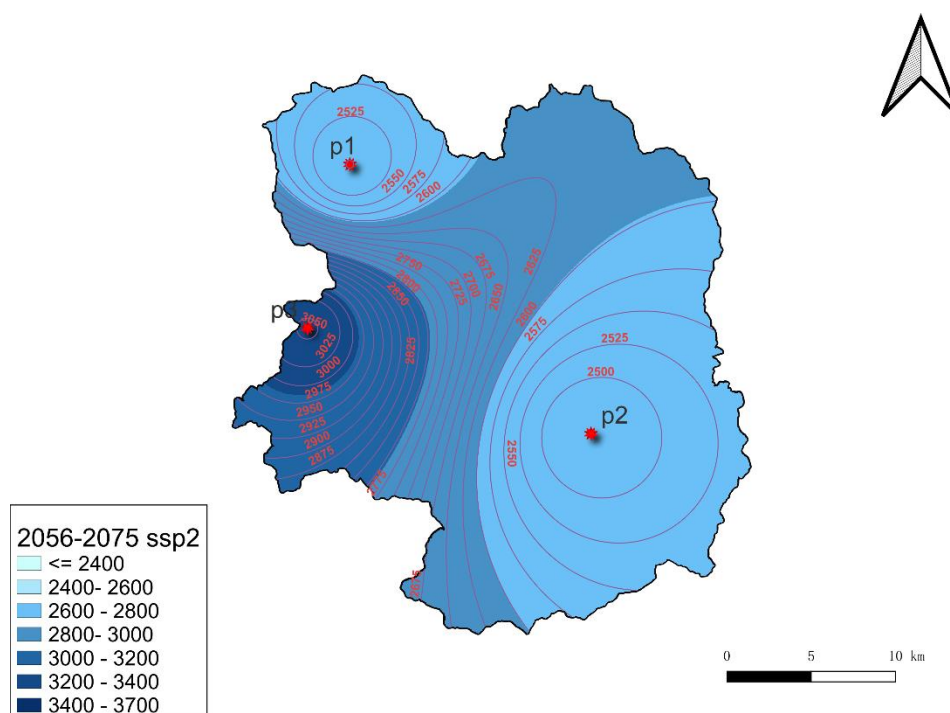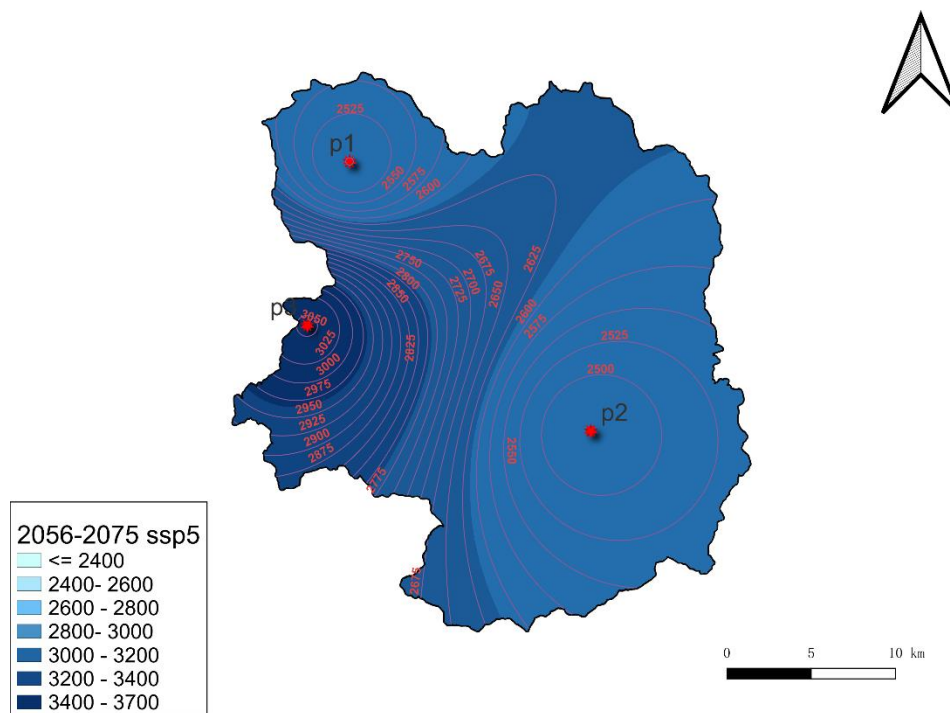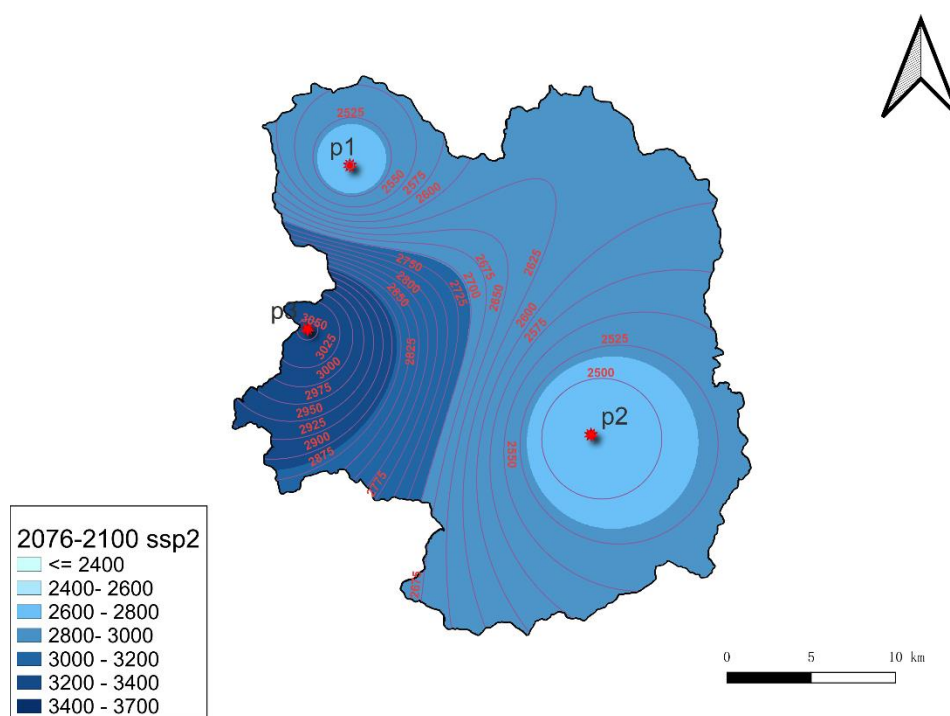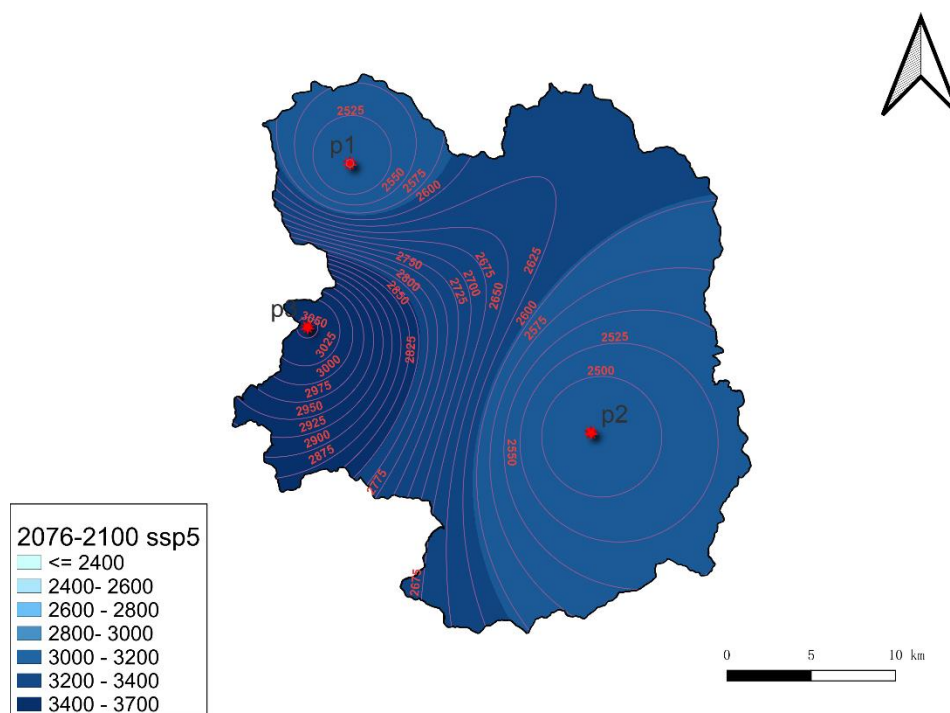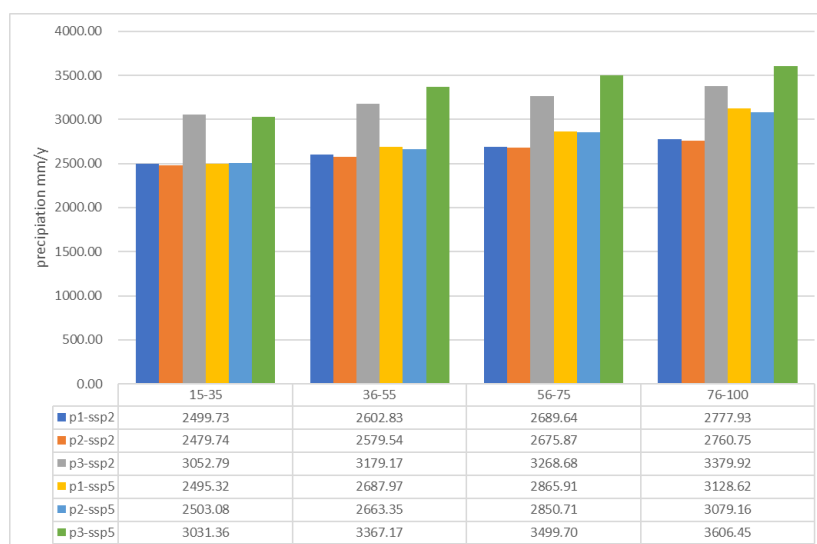
Figure 4.63:   Average of Annual Rainfall Pattern of Three Stations based on SSP2 -4.5 (2076-2100)

Figure 4.64:   Average of Annual Rainfall Pattern of Three Stations based on SSP5-8.5 (2076-2100)

According to Figures 4.57 to 4.64, precipitation changes correspond to contour variations, indicating a gradual migration of the coverage of high precipitation values from high-altitude zones to low-lying areas. Assuming a horizontal line drawn from point p3 and seeking the centre of Cameron Highlands as the coordinate origin, it can be observed that over time, the region with high precipitation values predominantly diverges from the southwest and spreads north-eastward. Despite higher rainfall in elevated areas and lower rainfall in low-lying areas, it does not necessarily imply that the likelihood of disasters in points p1 and p2 is lower than that in the p3 region. For instance, mudslides may be influenced by gravity and reach low-lying areas. Therefore, further disaster analysis should consider specific circumstances.

	15-35	36-55	56-75	76-100
p1-ssp2	2499.73	2602.83	2689.64	2777.93
p2-ssp2	2479.74	2579.54	2675.87	2760.75
p3-ssp2	3052.79	3179.17	3268.68	3379.92
p1-ssp5	2495.32	2687.97	2865.91	3128.62
p2-ssp5	2503.08	2663.35	2850.71	3079.16
p3-ssp5	3031.36	3367.17	3499.70	3606.45

Figure 4.65：Aggregated precipitation in (2015-2035), (2036-2055), (2056-2075), (2076-2100) of Three Stations based on SSP2-4.5 and SSP5-8.5

CHAPTER 5

CONCLUSION AND RECOMMENDATIONS

5.1 Conclusion

When comparing historical observed data with historical simulated data, it was observed that the model effectively simulated historical Tmax, Tmin, and Humidity values from 1983 to 2014, exhibiting consistency in terms of means, maximums, and minimums. However, the model showed limitations in adequately reproducing historical precipitation. For both study places 1 and 2, the simulated values exhibited consistent trends with observed values for average monthly precipitation. Nevertheless, concerning the maximum monthly precipitation, both places showed instances where the historical simulated precipitation significantly underestimated the observed values. Consequently, a bias correction using the Delta Method was applied to historical simulated precipitation. To demonstrate the model's robustness, statistical methods such as Probability Density Function (PDF), Prediction Accuracy, Index of Accuracy, RMSE analysis, ANOVA, etc., were employed to validate historical model data. The results indicated that the bias-corrected historical simulated precipitation aligned well with historical precipitation, reaffirming the reliability of the generated historical models related to Tmax, Tmin, and Humidity.

For the generated Local Climate Model (2015-2100), in terms of precipitation, study places 1 and 2, based on SSP2-4.5 and SSP5-8.5 scenarios, exhibited nearly identical precipitation changes. However, under these two emission scenarios, precipitation changes began to diverge notably from 2063 onwards. Conversely, for study place 3, precipitation changes based on both emission scenarios were significantly higher than those observed in places 1 and 2. Interestingly, emission scenarios did not seem to influence precipitation changes at study place 3, as the precipitation changes under the two scenarios remained intertwined from 2015 to 2100 without distinct separation.

In the study of anomalous precipitation for study places 1 and 2, there appeared to be no apparent correlation in anomalous precipitation under the SSP2-4.5 scenario. However, under the SSP5-8.5 scenario, a turning point in anomalous precipitation was observed around 2049, transitioning from negative anomalies to positive anomalies. Subsequently, positive anomalies exhibited a clear upward trend. In contrast, anomalous precipitation under the SSP2-4.5 scenario for both places continued to fluctuate significantly after 2049. These observations suggest that the impact of the SSP5-8.5 emission scenario on precipitation is much higher than that of the low emission scenario, and this impact may be less influenced by terrain, altitude, and non-human activities.

Spatial analysis of annual average precipitation was conducted for the three study places using QGIS software under the SSP2-4.5 and SSP5-8.5 scenarios. The contour map revealed that the elevation of study place 1 was 2520 meters, study place 2 was 2490 meters, and study place 3 was 3000 meters. Study places 1 and 2 were similar depressions, while study place 3 was a plateau with ridges extending in the northeast direction. With increasing altitude, a general trend of temperature decrease was observed. Colder air at higher altitudes may lead to water vapor condensation into clouds and eventual precipitation. Thus, in certain circumstances, high-altitude areas may experience higher precipitation, a phenomenon corroborated by the precipitation distribution map.

5.2 Recommendations

i.Deployment of Diverse Climate Models:
Employ multiple climate models to simulate scenarios and comprehend variations among them. This approach offers valuable insights into the diversity of model responses, contributing to a more comprehensive assessment.

ii.Exploration of Local Climate Mechanisms:
Delve into region-specific climate mechanisms that may induce disparities with general emission principles. This involves a meticulous examination of local

factors, topographical nuances, and non-human influences impacting climate outcomes.

iii. The incorporation of dynamic downscaling methods is anticipated to facilitate a more comprehensive capture of future climate dynamic variations, thereby enhancing the precision of simulated outcomes. This integrated approach holds promise in furnishing more dependable future precipitation simulations, consequently rendering the model's response to scenario-induced emissions changes more cogent.

REFERENCE

Benestad, R.E., 2004. Empirical-statistical downscaling in climate modeling. Eos, Trans. Am. Geophys. Union 85, 417–422.

Benestad, R., Sillmann, J., Thorarinsdottir, T.L., Guttorp, P., Mesquita, M. d S., Tye, M.R., Uotila, P., Maule, C.F., Thejll, P., Drews, M., Parding, K.M., 2017. New vigour involving statisticians to overcome ensemble fatigue. Nat. Clim. Change 7, 697–703. https://doi.org/10.1038/nclimate3393.

Banze, F., Guo, J., Xiaotao, S., 2018. Impact of climate change on precipitation in Zambeze River Basin in Southern Africa. Nature Environment and Pollution Technology 17 (4), 1093–1103.

Campozano, L., Tenelanda, D., Sanchez, E., Samaniego, E., Feyen, J., 2016. Comparison of statistical downscaling methods for monthly total precipitation: case study for the Paute river basin in Southern Ecuador. Adv. Meteorol. 2016. doi:10.1155/2016/6526341.

Chen Z., Guo J.H., Li W., Jia H.T., Liang X., Wang X.Q., Bao Z., 2023. Evaluating emission reduction potential at the "30-60 Dual Carbon targets" over China from a view of wind power under climate change. Science of the Total Environment, 900, 165782.

Ebenezer K.S., Edward A.A., Amos T.K., Nana Sarfo A.D., Komlavi A., Eric M.M., Mashael Y., 2023. Assessment of Shared Socioeconomic Pathway (SSP) climate scenarios and its impacts on the Greater Accra region. Urban Climate, 49,101432.

Frías, M.D., Zorita, E., Fern´ andez, J., Rodríguez-Puebla, C., 2006. Testing statistical downscaling methods in simulated climates. Geophys. Res. Lett. 33. https://doi. org/10.1029/2006GL027453.

Fowler, H.J., Blenkinsop, S., Tebaldi, C., 2007. Linking climate change modelling to impacts studies: recent advances in downscaling techniques for hydrological modelling. Int. J. Climatol. 27 (12), 1547–1578. https://doi.org/10.1002/joc.1556.

Giorgi, F., Gutowski, W.J., 2015. Regional Dynamical Downscaling and the CORDEX Initiative. Annu. Rev. Environ. Resour. 40 (1), 467–490. https://doi.org/10.1146/ annurev-environ-102014-021217.

Gulacha, M.M., Mulungu, D.M.M., 2016. Generation of climate change scenarios for precipitation and temperature at local scales using SDSM in Wami-Ruvu river basin Tanzania. Phys. Chem. Earth 100, 62–72. doi:10.1016/j.pce.2016.10.003.

Guo, J., Huang, G., Wang, X., et al., 2018. Dynamically-downscaled projections of changes in temperature extremes over China. Clim. Dynam. 50 (3), 1045e1066. https://doi.org/10.1007/s00382-017-3660-7

Gebrechorkos, S.H., Hülsmann, S., Bernhofer, C., 2019. Statistically downscaled climate dataset for East Africa, (2019) Sci. Data 6 (1), 1-8.

Humphrey, V., Gudmundsson, L., 2019. GRACE-REC: a reconstruction of climate-driven water storage changes over the last century. Earth Syst. Sci. Data. 11 (3), 1153–1170. https://doi.org/10.5194/essd-11-1153-2019.

IPCC, 2018. Summary for Policymakers. In: Global Warming of 1.5°C. An IPCC Special Report on the impacts of global warming of 1.5°C above pre-industrial levels and related global greenhouse gas emission pathways, in the context of strengthening the global response to the threat of climate change, sustainable development, and efforts to eradicate poverty [Masson-Delmotte. In: Maycock, T., Tignor, M., Waterfield, T. (Eds.), Lonnoy. Press.

Iwadra, M., Odirile, P. T., Parida, B. P., Moalafhi, D. B., 2019. Evaluation of future climate using SDSM and secondary data (TRMM and NCEP) for poorly gauged catchments of Uganda: the case of Aswa catchment. Theoretical and Applied Climatology 137 (3), 2029–2048.

Knutti, R., Sedla´ˇcek, J., 2013. Robustness and uncertainties in the new CMIP5 climate model projections. Nat. Clim. Change 3, 369–373. https://doi.org/10.1038/ nclimate1716.

Liu, Z., Xu, Z., Charles, S.P., Fu, G., Liu, L., 2011. Evaluation of two statistical downscaling models for daily precipitation over an arid basin in China. Int. J. Climatol. Int. J. Clim. 31. doi:10.1002/joc.2211.

Li J.F., Zhong W.Y., CHEN D.L., Zhen L., 2023. Assessment of total and extreme precipitation over central Asia via statistical downscaling: Added value and multi-model ensemble projection. Advances in Climate Change Research, 14, 62-74

Maraun, D., Wetterhall, F., Ireson, A.M., Chandler, R.E., Kendon, E.J., Widmann, M., Brienen, S., Rust, H.W., Sauter, T., Themeßl, M., Venema, V.K.C., Chun, K.P., Goodess, C.M., Jones, R.G., Onof, C., Vrac, M., Thiele-Eich, I., 2010. Precipitation downscaling under climate change: recent developments to bridge the gap between dynamical models and the end user. Rev. Geophys 48. https://doi.org/10.1029/2009RG000314.

Matthew, O. J., Abiye, O. E., 2017. Evaluation of SDSM Performance in Simulating Rainfall and Temperature over Nigeria. Br. J. Appl. Sci. Technol 20, 1–15

N.D. Bennett, et al., Characterising performance of environmental models, Environ. Model. Software 40 (2013) 1–20, https://doi.org/10.1016/j. envsoft.2012.09.011.

Norsyuhada, W., Marlinda Abdul Malek, Reba, Nuratiah Zaini, Ali Najah Ahmed, Sherif, M. and El-Shafie, A. (2023). Rainfall-runoff modelling based on global climate model and tropical rainfall measuring mission (GCM -TRMM): A case study in Hulu Terengganu catchment, Malaysia. *Heliyon*, 9(5), pp.e15740–e15740. doi: https://doi.org/10.1016/j.heliyon.2023.e15740.

Pierce, D.W., Cayan, D.R., Thrasher, B.L., 2014. Statistical Downscaling Using Localized Constructed Analogs (LOCA). J. Hydrometeorol. 15, 2558–2585. https://doi.org/ 10.1175/JHM-D-14-0082.1.

Sun, A.Y., Scanlon, B.R., Zhang, Z., Walling, D., Bhanja, S., Mukherjee, A., Zhong, Z., 2019. Combining physically-based modeling and deep earning for fusing GRACE satellite data: can we learn from mismatch? Water Resour. Res. 55 (2), 1179–1195. https://doi.org/10.1029/2018WR023333.

Siabi, E.K., Kabobah, A.T., Akpoti, K., Anornu, G.K., Amo-Boateng, M. and Nyantakyi, E.K. (2021). Statistical downscaling of global circulation models to assess future climate changes in the Black Volta basin of Ghana. *Environmental Challenges*, 5(100299), p.100299. doi: https://doi.org/10.1016/j.envc.2021.100299.

Timbal, B., Li, Z., Fernandez, E., 2008. The Bureau of Meteorology Statistical Downscaling Model Graphical User Interface: user manual and software documentation, CAWCR Technical Report No. 004.

Tryhorn, L., Degaetano, A., 2011. A comparison of techniques for downscaling extreme precipitation over the Northeastern United States. Int. J. Climatol. 31, 1975–1989. doi:10.1002/joc.2208.

Tavakol-Davani, H., Nasseri, M., Zahraie, B., 2013. Improved statistical downscaling of daily precipitation using SDSM platform and data-mining methods. Int. J. Climatol. 33, 2561–2578. doi:10.1002/joc.3611.

Turco, M., Llasat, M.C., Herrera, S., Guti´errez, J.M., 2017. Bias correction and downscaling of future RCM precipitation projections using a MOS-Analog technique. J. Geophys. Res. Atmospheres 122, 2631–2648. https://doi.org/10.1002/ 2016JD025724.

Tang J., Song P.H., Hu X.J., Chen C.Y., Wei B.J., Zhao S.W., 2023. Coupled effects of land use and climate change on water supply in SSP–RCP scenarios: A case study of the Ganjiang River Basin, China. Ecological Indicators, 154, 110745.

USNEWS, N., 2022.10 of the Deadliest Natural Disasters in 2022.

Vrac, M., Stein, M.L., Hayhoe, K., Liang, X.-Z., 2007. A general method for validating statistical downscaling methods under future climate change. Geophys. Res. Lett. 34. https://doi.org/10.1029/2007GL030295.

Wilby, R. L., Wigley, T. M., 1997. Downscaling general circulation model output: a review of methods and limitations. Progress in physical geography 21 (4), 530–548.Chicago. doi:10.1177/030913339702100403.

Wilby, R.L., Dawson, C.W., 2007. SDSM 4.2-A decision support tool for the assessment of regional climate change impacts. User Manual 94 (1), 1–94 Lancaster University Lancaster/Environment Agency England and Wales, UK.

Wilby, R.L. and Dawson, C.W., 2013. The Statistical DownScaling Model: insights from one decade. International Journal of Climatology, 33, pp.1707–1719. [Online] Available at: https://doi.org/10.1002/joc.3544.

Wilby, R.L., Dawson, C.W., Murphy, C., O'Connor, P., Hawkins, E., 2014. The statistical downscaling model -decision centric (SDSM-DC): conceptual basis and applications. Clim. Res. 61, 251–268. doi:10.3354/cr01254.

Wu, J., Han, Z., Xu, Y., et al., 2020. Changes in extreme climate events in China under 1.5 ———————— Ce4 ———————— C global warming targets: projections using an ensemble of regional climate model simulations. J. Geophys. Res. Atmos. 125 (2), e2019JD031057. https://doi.org/10.1029/2019JD031057.

Wang L., Li Y., Li M., Li L.C., Liu F.G., Liu D.L., Bakhtiyor P., 2022. Projection of precipitation extremes in China's mainland based on the statistical downscaled data from 27 GCMs in CMIP6. Atmospheric Research, 280, 106462.

Xu, C.-Y., 1999. Climate change and hydrologic models: a review of existing gaps and recent research developments. Water Resour. Manag. 13, 369–382. https://doi. org/10.1023/A:1008190900459.

Xu, Z., Han, Y., Yang, Z., 2019. Dynamical downscaling of regional climate: A review of methods and limitations. Sci. China Earth Sci. 62, 365–375. https://doi.org/ 10.1007/s11430-018-9261-5.

Yin, W., Hu, L., Zhang, M., Wang, J., Han, S.C., 2018. Statistical downscaling of GRACE-derived groundwater storage using ET data in the North China plain. J. Geophys. Res-Atmos. 123 (11), 5973–5987. https://doi.org/10.1029/2017JD027468.